KLOE Note 177
April 2002

Measurement of the visible production cross section $\sigma(e^+e^- \to \phi \to \eta\gamma)$ with η decaying to $\gamma\gamma$ and $\pi^0\pi^0\pi^0$

S. Giovannella, S. Miscetti

INFN - Laboratori Nazionali di Frascati

Abstract

In this note we report the measurement of the visible cross sections for the reaction $e^+e^- \to \phi \to \eta\gamma$, with η decaying into $\gamma\gamma$ or $\pi^0\pi^0\pi^0$, using a sample of 16 pb^{-1} collisions collected at the ϕ resonance peak. We obtain $\sigma(\phi \to \eta\gamma \to \gamma\gamma\gamma) = (17.07 \pm 0.05_{\mathrm{stat}} \pm 0.44_{\mathrm{syst}})$ nb and $\sigma(\phi \to \eta\gamma \to \pi^0\pi^0\pi^0\gamma) = (13.82 \pm 0.05_{\mathrm{stat}} \pm 0.47_{\mathrm{syst}})$ nb. The ratio of these cross sections provide a measurement of $R = \mathrm{BR}(\eta \to \gamma\gamma)/\mathrm{BR}(\eta \to 3\pi^0)$ of $0.810 \pm 0.026_{\mathrm{stat+syst}}$ in good agreement with the PDG values. The visible production cross-section of the ϕ meson at the *phi* peak is also determined to be: $\sigma_\phi = (3.34 \pm 0.01_{\mathrm{stat}} \pm 0.12_{\mathrm{syst}})$ μb.

1 Introduction

Altough in KLOE most of the measurements are obtained trough ratio of branching ratios, BR, the determination of the ϕ cross section is useful to normalize the rate of the rare ϕ decays (such as the radiative transitions $\phi \to a_0\gamma/f_0\gamma$) without needing to restream specific channels with higher rate on the same sample. We have therefore searched for $\phi \to \eta\gamma$, with η decaying either to $\gamma\gamma$ or $\pi^0\pi^0\pi^0$, in order to determine this visible cross-section. This study also provides a clean sample of multiphoton events, where the systematics on photon counting is addressed.

For this analysis, we have considered only the runs taken in November and December 2000 ($15174 \div 17330$) having a measurement of the luminosity performed with VLAB [1]. The whole sample (sample A) corresponds to an integrated luminosity (L_{int}) of (16.0 ± 0.3) pb^{-1}.

As reported in Ref. [2], we have found an unexpected event loss of $\sim 9\%$ due to the standard event classification selection (ECL) for neutral radiative decays. For this reason, we have restreamed all the sample starting from events after the FILFO background rejection (FLF), using a very loose radiative filter (NRLOOSE) with efficiency higher than 99% for the two processes under consideration.

2 Reconstruction of prompt photons

2.1 Description of clustering procedure

Since this analysis is based on calorimetry, a more detailed description of the clustering algorithm is given. Using the timing (t) and energy (e) information collected on each cell and its geometrical location, the space hits ($\vec{r}$, t, e) are built. The calorimeter reconstruction builds objects called preclusters by joining contiguous hits in the transverse plane. For each precluster the total energy (E) is obtained summing the energy of the collected hits while the centroids of the space points ($\vec{R}$) and of the timing (T) are calculated as energy weighted averages of the information of the joined cells. A breaker procedure uses the r.m.s of the timing to separate preclusters composed by two particles impinging along the fibers on the same transversal regions. A cluster is then formed by merging the preclusters having $\Delta R < 40$ cm and $|\Delta T| < 2.5$ ns, being R the distance between the average interaction point and the clusters centroid. A theshold of 3 MeV is then applied.

2.2 Recovering procedure for cluster splitting

Comparing data and Montecarlo (MC) samples of $e^+e^- \rightarrow \gamma\gamma$, where a tight selection has been applied on the two main clusters, we have controlled the production of the shower fragments (splitted clusters). In Fig. 1.top (bottom) the scatter plots of ΔR vs ΔT and ΔR_T vs ΔZ are shown for the data (MC) sample; the differences are between one of the main clusters and all the fragments of the event. The situation is more understandable if considering only the projections: in Fig. 2.top-left the distribution of ΔR is shown with the blue points representing data and the red line the expected MC contribution. While the normalization at large ΔR is correct (which also means that $e^+e^- \rightarrow \gamma\gamma(\gamma)$ is reasonably described by the MC generator [3]) a large discrepancy is observed at low values of ΔR. Similarly, in Fig. 2.top-right the distribution of ΔT shows a large unexpected contribution

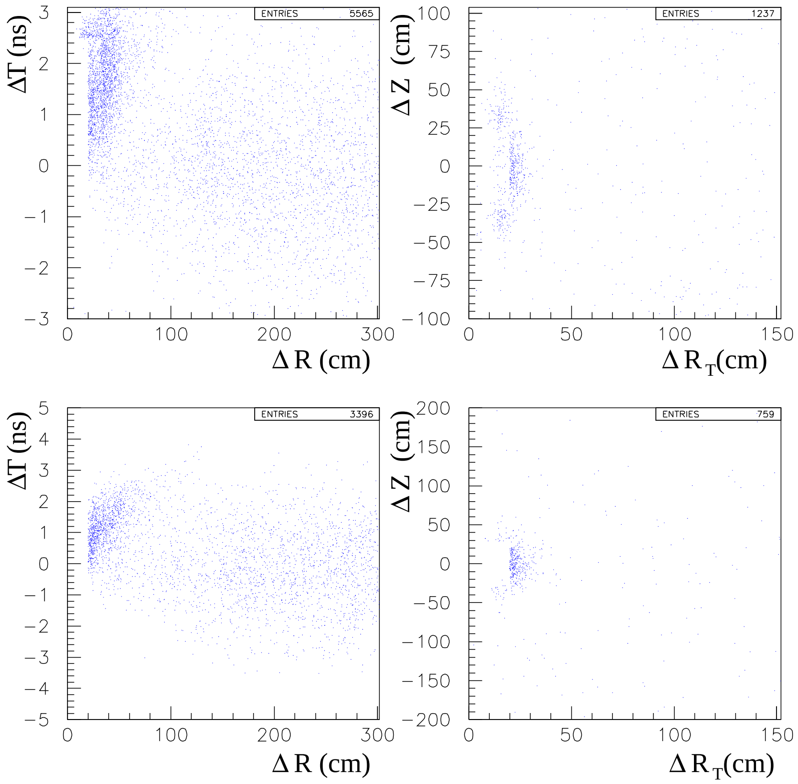

Figure 1: Cluster fragment distributions: ΔR vs ΔT (left) and ΔR_T vs ΔZ (right) for data (top) and MC (bottom).

at positive values above 2 ns. In Fig. 2.bottom the energy spectrum of the closest fragment is also shown; black points are data and red line is MC. The discrepancy is located at energy below 50 MeV. We believe that this effect is not due to accidental contamination since the MC well reproduces the negative tail of ΔT but it is instead related to the different time and space resolutions between data–MC which can play some role in the breaker procedure.

After hardening the merging procedure by joining clusters with $\Delta R < 1.5\ \mathrm{cm}/\sqrt{E\,(\mathrm{GeV})}$ and $|\Delta T| < 3.5$ ns the situation improves. This is clearly shown in Fig. 3 where the ΔR, ΔT and energy distributions exhibit a much better data–MC agreement. The effect of such a procedure in merging photons depends on the event topology and has to be evaluated for each specific channel.

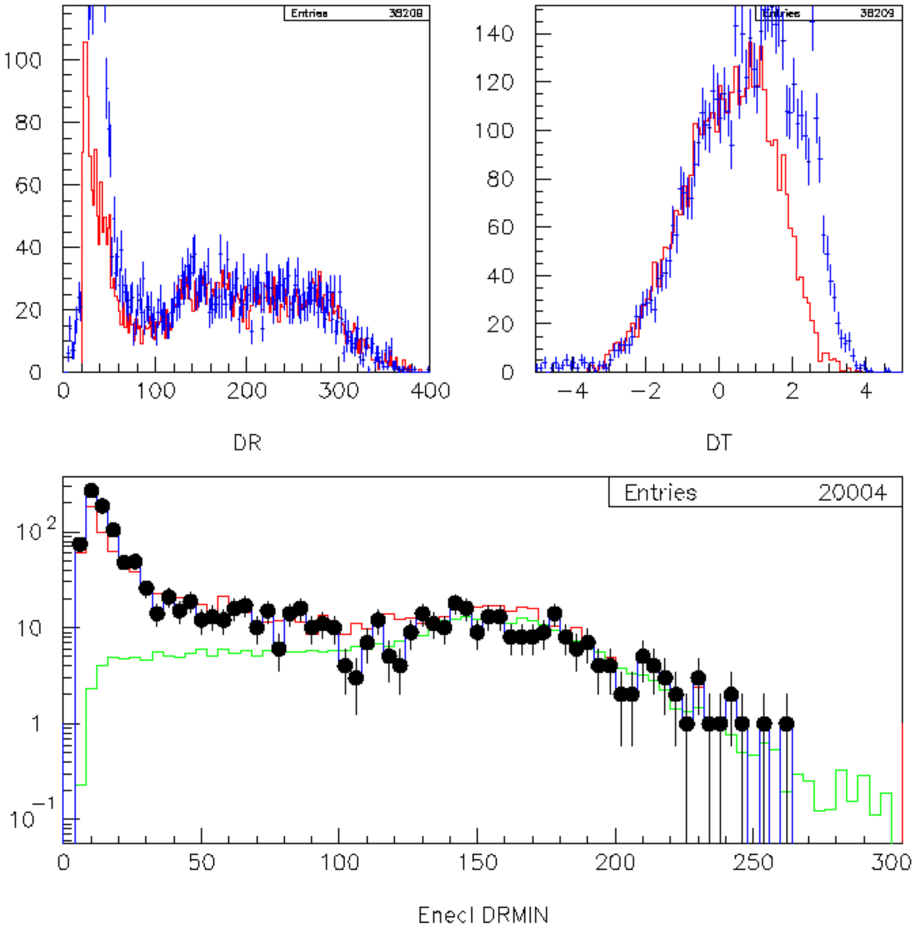

Figure 2: Cluster fragment distributions before the new merging procedure: ΔR (top-left), ΔT (top-right) and cluster energy of the closest fragment (bottom). Blue hitograms and black dots are data, red and green hitograms are $e^+e^- \to \gamma\gamma$ and $\phi \to \eta\gamma/\pi^0\gamma \to \gamma\gamma\gamma$ MC events respectively.

2.3 Cluster efficiency

The cluster reconstruction efficiency, ϵ_{clu}, is measured using two different control samples: $e^+e^- \to e^+e^-\gamma$ and $e^+e^- \to \rho\pi \to \pi^+\pi^-\pi^0$. In Fig. 4.left the distribution of ϵ_{clu} for the data (blue dots) and MC (green dots) is reported for different polar angle θ_γ of the radiative photon. The method shown is the one based on $e^+e^- \to e^+e^+\gamma$ and developed together with G.Cabibbo [4]. The efficiency is 90% at 20 MeV, reaching 100% above

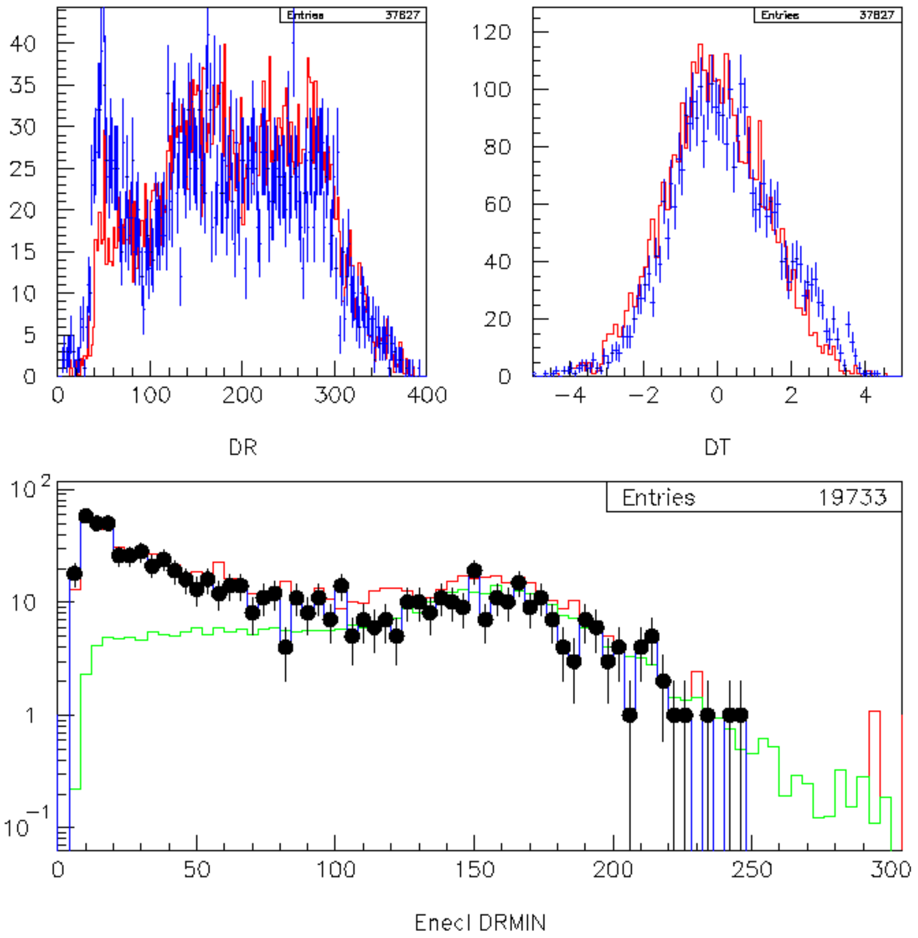

Figure 3: Cluster fragment distributions after the new merging procedure: ΔR (top-left), ΔT (top-right) and cluster energy of the closest fragment (bottom). Blue hitograms and black dots are data, red and green hitograms are $e^+e^- \rightarrow \gamma\gamma$ and $\phi \rightarrow \eta\gamma/\pi^0\gamma \rightarrow \gamma\gamma\gamma$ MC events respectively.

70 MeV.

The MC expectations have been evaluated adding a description of the ADC thresholds in the simulation. In Fig. 5.top-left the cell energy, $E_{\rm cell}$, distribution is shown for data (points) and MC (solid line) after proper normalization at $E_{\rm cell} > 20$ MeV. It is evident that the Montecarlo does not describe the cutoff at low energy and we can correct for this using the curve of cell efficiency, $\epsilon_{\rm cell}$, (Fig. 5.top-right) obtained normalizing the $E_{\rm cell}$

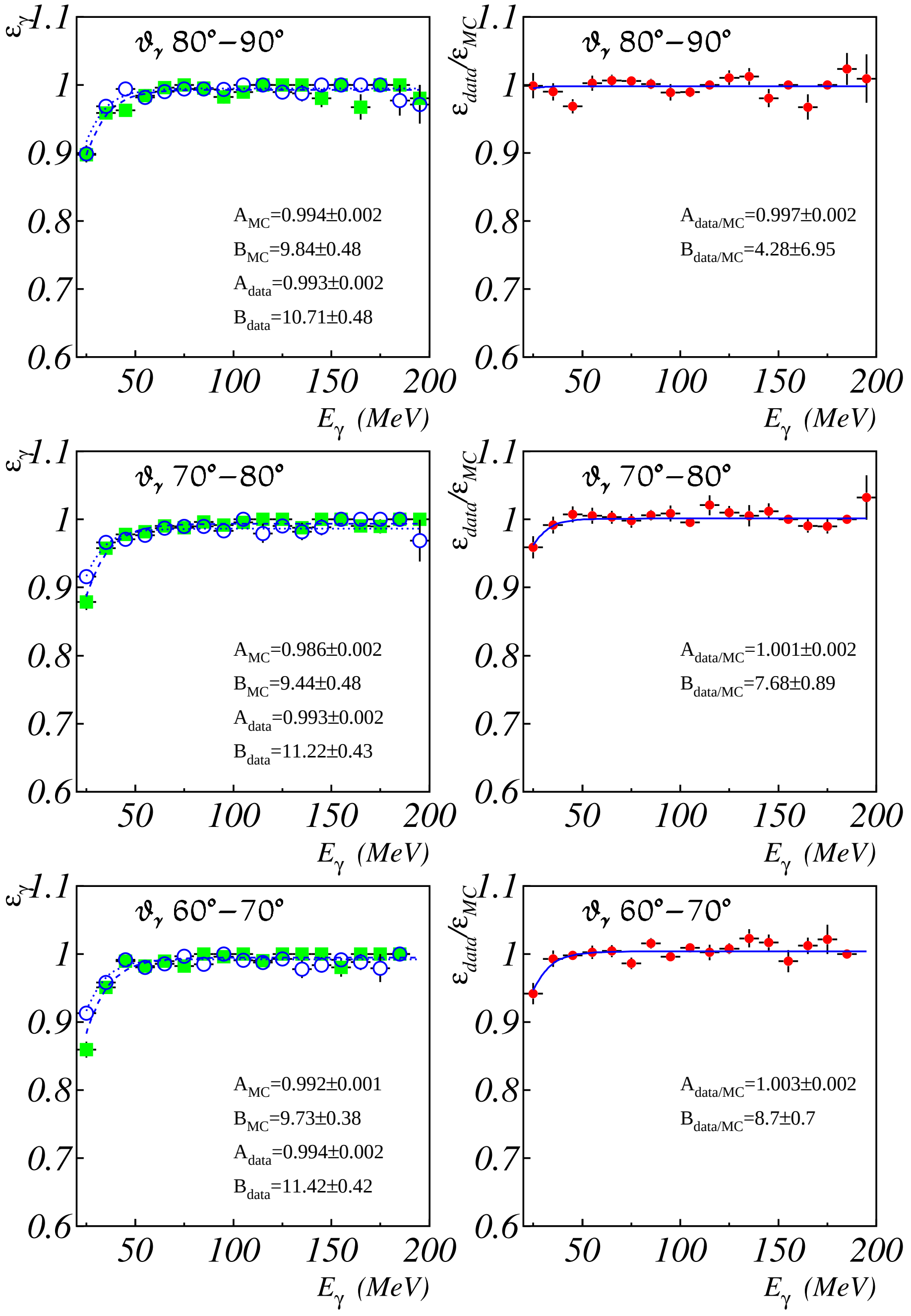

Figure 4: Distributions of $\epsilon_{\rm clu}$ as measured using a $e^+e^- \to e^+e^-\gamma$ sample for three different values of θ_γ: $80° < \theta_\gamma < 90°$ (top), $70° < \theta_\gamma < 80°$ (middle) and $60° < \theta_\gamma < 70°$ (bottom). On the left side the efficiency as a function of the energy of the photon for data (blue dots) and MC (green dots) is shown; on the right the ratio between the values obtained for MC and data is displayed vs E_γ.

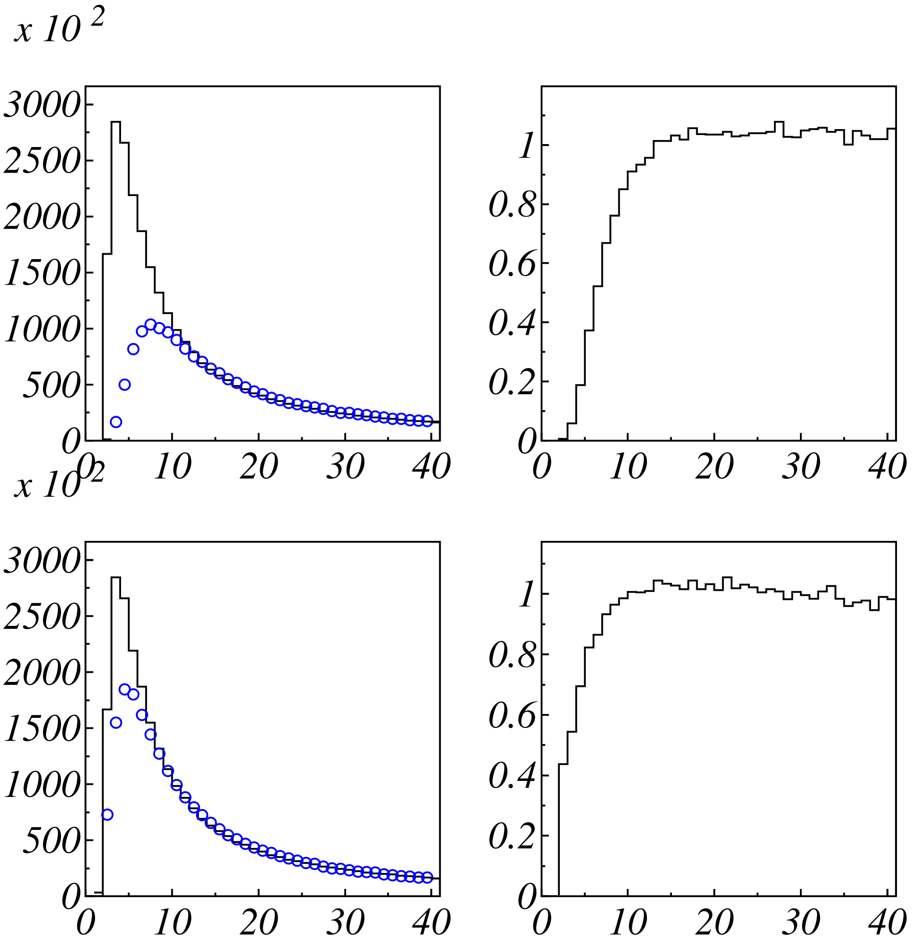

Figure 5: ADC thresholds of summer 2000 (top) and end 2000 (bottom) data taking. On the left side the cell energy distributions for data (blu circles) and MC (solid) are shown; on the right the ratio between data and MC is displayed vs $E_{\rm cell}$.

distribution of MC with data. After this correction, the simulation follows closely the $\epsilon_{\rm clu}$ behaviour in the data altough discrepancies at a level of few % are still available at energy below 40 MeV.

The $\epsilon_{\rm cell}$ curve shown here has been measured in summer 2000 before increasing the EMC HV. We refer to this curve as (a). To take into consideration the effect of HV increase we show in Fig. 5.bottom the $\epsilon_{\rm cell}$ curve after this operation have been done. We refer to this curve as (b). This curve is also the default one used in this analysis.

2.4 Prompt photon definition

The timing scale is set using $e^+e^- \to \gamma\gamma$ events with an average precision of few tens of picoseconds. A residual dependence of the timing along the fiber coordinates, up to 300 ps, is still observed due to the timing walk on pulse-height; an ad-hoc correction reduces this effect below 100 ps. A prompt photon is then defined as a neutral particle, *i.e.* a cluster without any close track extrapolation, satisfying the prompt time window requirement of $|T - R/c| < \mathrm{MIN}(5\,\sigma_T, 2\,\mathrm{ns})$.

2.5 Contamination due to accidental clusters

The presence of accidental clusters due to machine background is controlled looking at out-of-time particles. In the used sample we have measured a rate per event of spurious background clusters of $(87 \pm 13)\%$ [5]. These accidentals show a soft spectrum and are peaked at small polar angles. The usage of the prompt time window reduces this contamination to below 1.8%. Due to the high level of background contamination ($\sim 8\%$ in time window) the QCAL detector was not used in this analysis, thus forcing us to exclude the region with $\theta_\gamma < \theta_{\gamma\,\mathrm{cut}} = 21^\circ$. A description of the machine background is anyhow used in the MC by adding to the EMC out of time hits taken in the data to the generated hits [6].

2.6 Precision on the energy scale setting

In order to set the energy scale, we use the sample of $e^+e^- \to \gamma\gamma$ selected online by the L3BHA circular buffer [7]. In doing so, we restricted our calibration sample in the endcaps to use only the clusters produced with $R_T \geq 130$ cm. The average precision of the scale setting is at a level of 0.3% as shown by comparing to PDG the average values of the reconstructed mass for π^0, η and K_S [8]. However, a residual systematic effect on the energy scale is still present in the endcaps as shown by Fig. 6.bottom-right. In this plot we display, for an $e^+e^- \to \gamma\gamma$ sample, the distribution of the mean energy $\langle E \rangle$ as a function of R_T. As expected, whenever integrating in the region with $R_T > 130$ cm we correctly obtain the setting value of 510 MeV. However, a linear dependence of $\langle E \rangle$ on R_T is observed. This is a large effect, corresponding to a ${}^{+10/510}_{-20/510}$ deviation of the correct energy scale. This problem is related to the correction for the light-attenuation along the

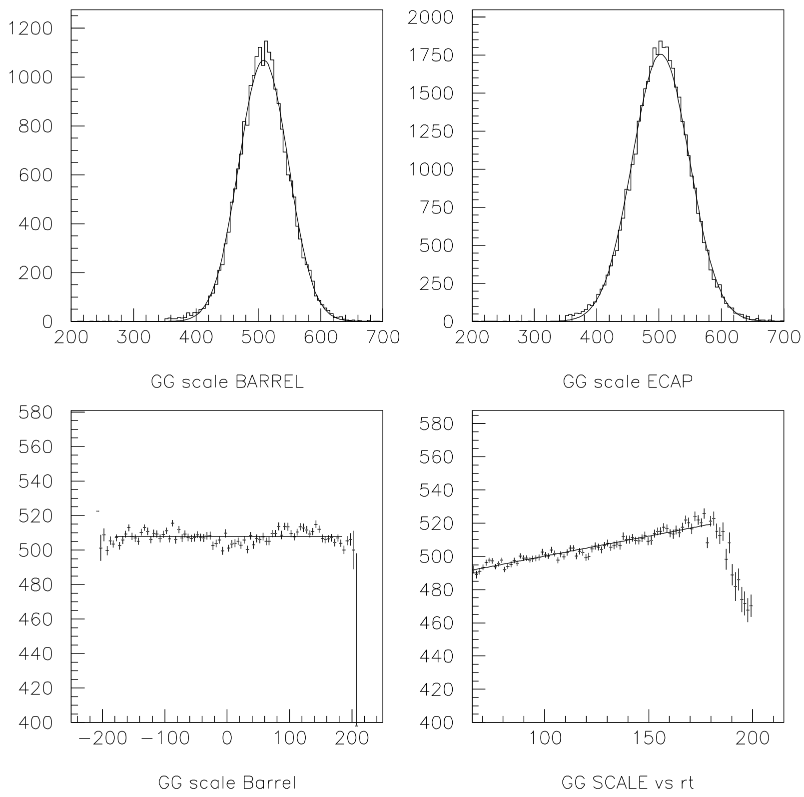

Figure 6: Scale setting for barrel (top) and endcaps (bottom): energy of the clusters for $e^+e^- \to \gamma\gamma$ events (top) and its dependence as a function of the position alonf the fibers (bottom).

fibers in the endcaps since the determination of $\lambda_{\rm att}$ is here not so precise as in the barrel. In this analysis, we have corrected for the residual dependence on the endcaps, without observing a relevant change on photon counting.

3 The $\phi \to \eta\gamma \to \gamma\gamma\gamma$ decay

3.1 Kinematic fit

The decay $\phi \to \eta\gamma$ with $\eta \to \gamma\gamma$ is characterized by a radiative photon with energy $E_{\gamma_{\rm rad}} = 363$ MeV and by two photons from the η having a flat energy spectrum ranging in within (150$\div$ 500) MeV (Fig. 7.top). As a first analysis step, we require three prompt photons with $E \geq 7$ MeV produced in the polar angular region $21^\circ \leq \theta_\gamma \leq 159^\circ$. On this starting sample we perform a kinematic fit for the three possible combination of photons by requiring:

- **Energy and momentum conservation at the origin**
  $E_3 = E_\phi$, $\vec{P}_3 = \vec{P}_\phi$ where E_3, $\vec{P}_3$ are the sum of the energy and momenta for the three photon candidates and E_ϕ, $\vec{P}_\phi$ are the energy and momentum of the ϕ meson. For each run, we use the average values of the interaction point and of $\vec{P}_\phi$ as determined by the online procedure [9].

- **Constraint on the time of flight**
  The measured arrival time, T, is constrained to give the expected time of flight, R/c. This requirement does not modify the photon energies but helps on correcting the cluster positions.

- **Constraint on the η invariant mass**
  $M_{\gamma\gamma} = M_\eta$, where $M_{\gamma\gamma}$ is the invariant mass of the two photons assigned to η.

The smaller χ^2 is then chosen. The efficiency of selecting the right photon combination with this procedure (ϵ_{fit}) results to be very high in the Montecarlo: $\epsilon_{\text{fit}} > 99\%$. The fit corresponds to a degrees of freedom ndof = $\text{N}_{\text{constraints}} = 8$ and improves the energy resolution up to 0.3%, while slightly modifies the starting values of the cluster positions. For the χ^2 we have used different resolutions in data and MC, both measured on the corresponding sample.

3.2 Background rejection

In this search, we expect to have a small contamination due to the decay $\phi \to \pi^0\gamma$ with a signal to background ratio (S/B) of ~ 4. For this reason, the kinematic fit is also performed for the $\pi^0\gamma$ combination, imposing the constraing on the π^0 mass. For this process, the energy of the radiative photon is of ~ 500 MeV while the energy spectrum of the γ's from π^0 is flat from the threshold up to 500 MeV (see Fig. 7.bottom).

Other smaller contamination can be expected if we consider $e^+e^- \to \gamma\gamma$ with other photons produced either by higher order QED processes or residual cluster splitting. Similar

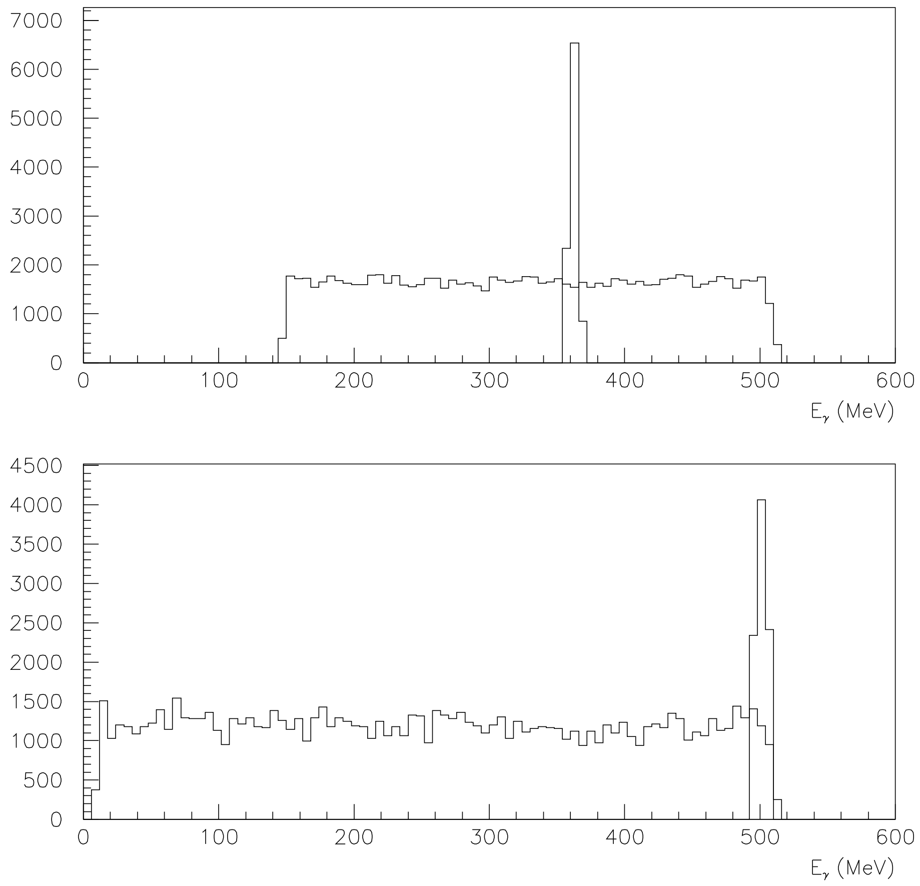

Figure 7: Energy spectra for $\phi \to \eta\gamma$ (top) and $\phi \to \pi^0\gamma$ (bottom). The peaked histograms are the energy of the radiative photons.

consideration can apply also to Bhabha events if, for any reason, there is some inefficiency on the drift chamber along the time.

The background rejection is based on simple kinematic considerations. In Fig. 8.top the distribution of the energy difference of the two photons assigned to η (γ_1, γ_2), ΔE, is shown for the data (black dots), the sum of expected signal and background from MC (red line) and from the expected background only (green line). Similarly, in Fig. 8.bottom the scatter plot of the γ_1, γ_2 opening angle ($\cos\theta_{12}$) vs ΔE is shown. It is clear that the background tends to assign as photons from the η the clusters which are almost back to back and with an high value of ΔE. In both plots, the red and blue arrows show the cuts used in the following for the evaluation of the background contamination ($\Delta E\text{cut}_1$, $\Delta E\text{cut}_2$).

To show the quality of the kinematic fit performed, in Fig. 9 the χ^2 distribution is reported both for data and MC, for the events without ΔE cut (top), with $\Delta E\text{cut}_1$ (middle) and with $\Delta E\text{cut}_2$ (bottom). We apply a cut of $\chi^2 \leq 30$ in the following. To calibrate the percentange of $\pi^0\gamma$ background, we use the fit in both $\eta\gamma$ and $\pi^0\gamma$ hypotheses. In Fig. 10.top-left the scatter-plot of $\chi^2_{\pi\gamma}$ vs $\chi^2_{\eta\gamma}$ is reported for data without any ΔE cut. In Fig. 10.top-right the same scatter plot is reported for simulated $\eta\gamma$ (blue points) and $\pi^0\gamma$ (green points) events; it is evident the contamination in the data appearing as the band at lower $\chi^2_{\pi\gamma}$ and higher $\chi^2_{\eta\gamma}$. In Fig. 10.bottom the distribution of $\chi^2_{\pi\gamma}$ for the data (black dots) is compared with the expected one for MC. In order to have a good data-MC comparison, the expected number of $\phi \to \pi^0\gamma$ events has been increased of 25% ($BR(\phi \to \pi^0\gamma) = 1.55 \times 10^{-3}$).

In the following we show few selected plots to compare the behaviour of the angular distributions between data and MC; in all of them black dots represent data while the green (red) line represents the background (background+signal) expected contribution. In Fig. 11.top (11.bottom) the distributions of $\cos\theta_{1R}$ ($\cos\theta_{12}$) are reported; 1–2 and R represent the η and the radiative photon clusters respectively. The same plots are shown in Fig. 12 after applying the ΔE cuts. Finally, in Fig. 13 the distribution of $\cos\theta_{max}$ is reported for all photons (top-left), the η-photons (top-right) or the radiative photon (bottom). In all cases, the agreement is excellent.

3.3 Evaluation of systematic errors

This analysis uses a very clean sample and the losses and discrepancy from the simulation are really small. Anyhow, we address the few sources of systematic errors in the following. We remind that all efficiencies have been evaluated at the end of the whole analysis chain, *i.e.* after requiring three prompt photons in acceptance and applying the χ^2 and ΔE cuts.

- **Trigger losses and Cosmic Veto**
  Since there are at least three clusters with $E > 150$ MeV, the ϕ-trigger is always satisfied ($> 99.9\%$ in MC). The only possible loss is due to the cosmic veto: in 16 pb^{-1} we observe 20 events out of 164 059 candidates. Scaling this number up for the prescaling factor of 50 used to filter these events, we estimate a probability of

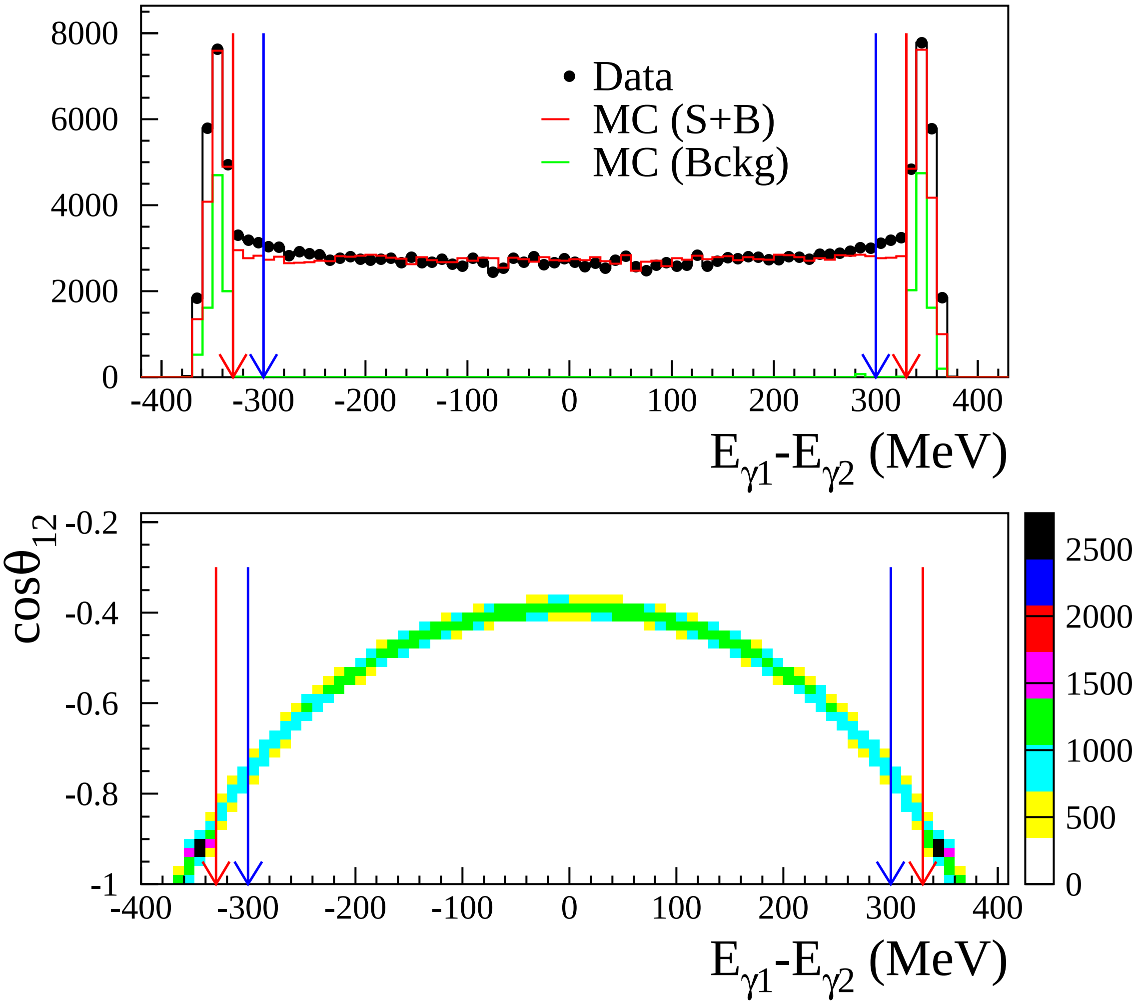

Figure 8: Energy difference of the two photons assigned to η (top) and its distribution as a function of the corresponding opening angle for MC events (bottom). The arrows show the ΔE cuts used in the analysis.

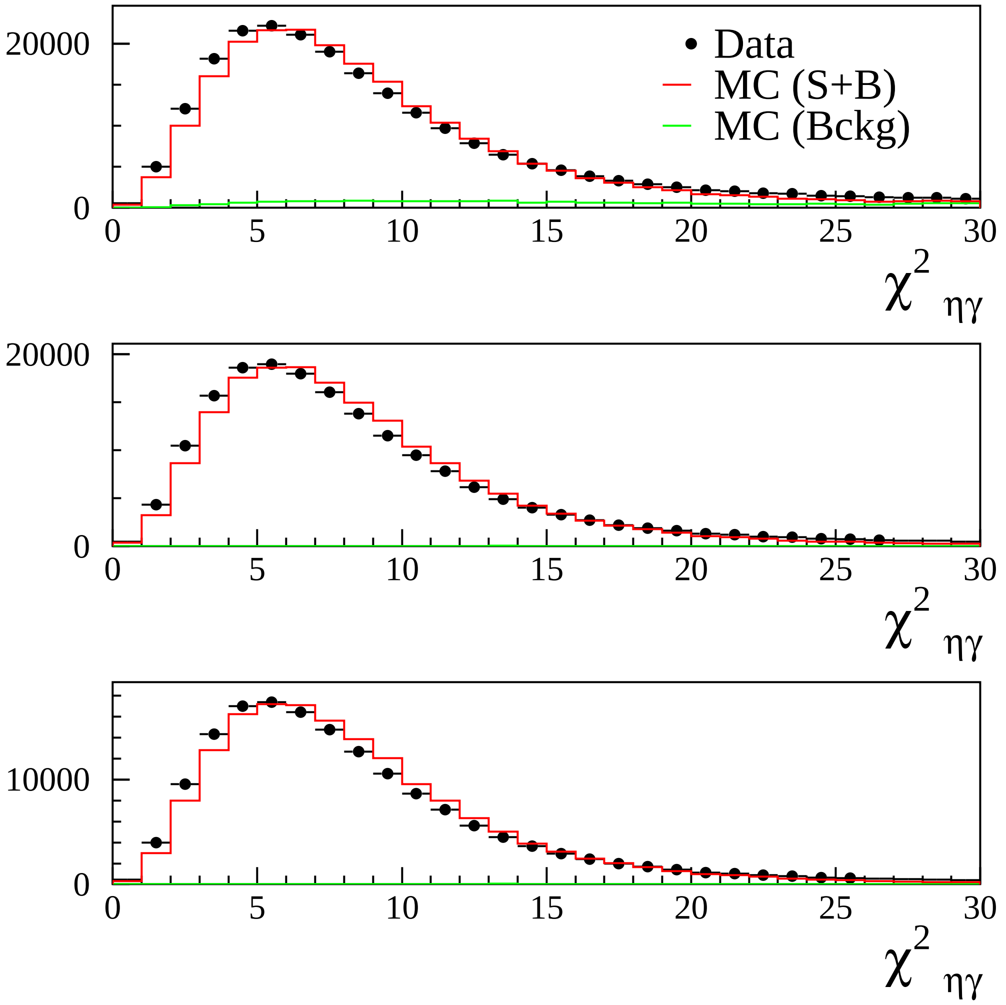

Figure 9: χ^2 distributions for $\phi \to \eta\gamma \to \gamma\gamma\gamma$ events with different background rejection: no ΔE cut (top), $|\Delta E| < 330$ MeV (middle) and $|\Delta E| < 300$ MeV (bottom). Data are the black points, MC is the red line and the green line shows the expected background.

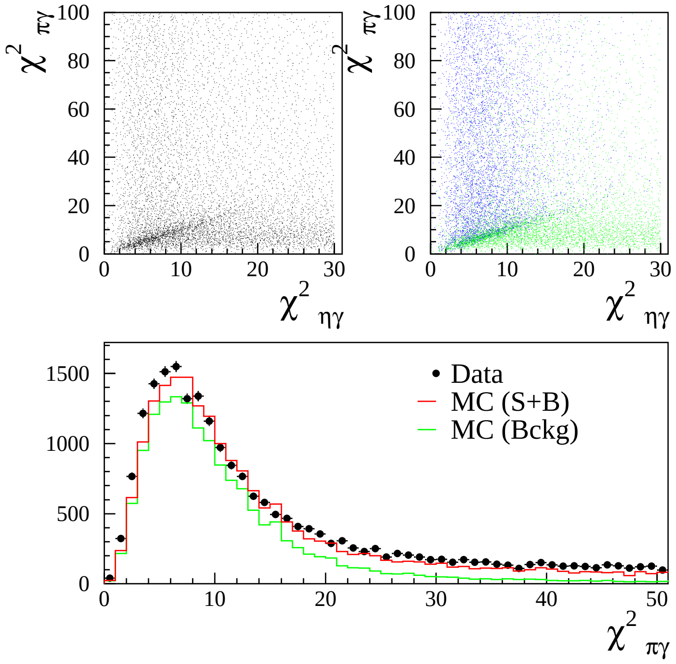

Figure 10: $\chi^2_{\pi\gamma}$ vs $\chi^2_{\eta\gamma}$ for data (top-left) and MC (top-right). $\phi \to \eta\gamma$ and $\phi \to \pi^0\gamma$ events are displayed in blue and green respectively. After increasing the expected $\phi \to \pi^0\gamma$ sample by 25%, a good data–MC agreement is found in the $\chi^2_{\pi\gamma}$ distribution (bottom).

event loss of: $(6.1 \pm 1.4) \times 10^{-3}$. In the simulation the corresponding loss is almost a factor two higher resulting $(12.2 \pm 0.3) \times 10^{-3}$.

- **Filfo and NRLOOSE losses**

  We determine by MC a 0.65% (0.45%) inefficiency due to Filfo (NRLOOSE) filter. We consider negligible such losses and we did not restream the events from raw data. We apply a conservative 0.5% relative systematic error to this preselection.

- **Cluster counting**

  The counting of cluster could be the source of a relevant error since the only requirement of three prompt γ's corresponds to a selection efficiency of 73%. Anyhow, this effect is negligible for this analysis. As shown in Par. 2.3, the $\epsilon_{\rm clu}$ reaches a 100%

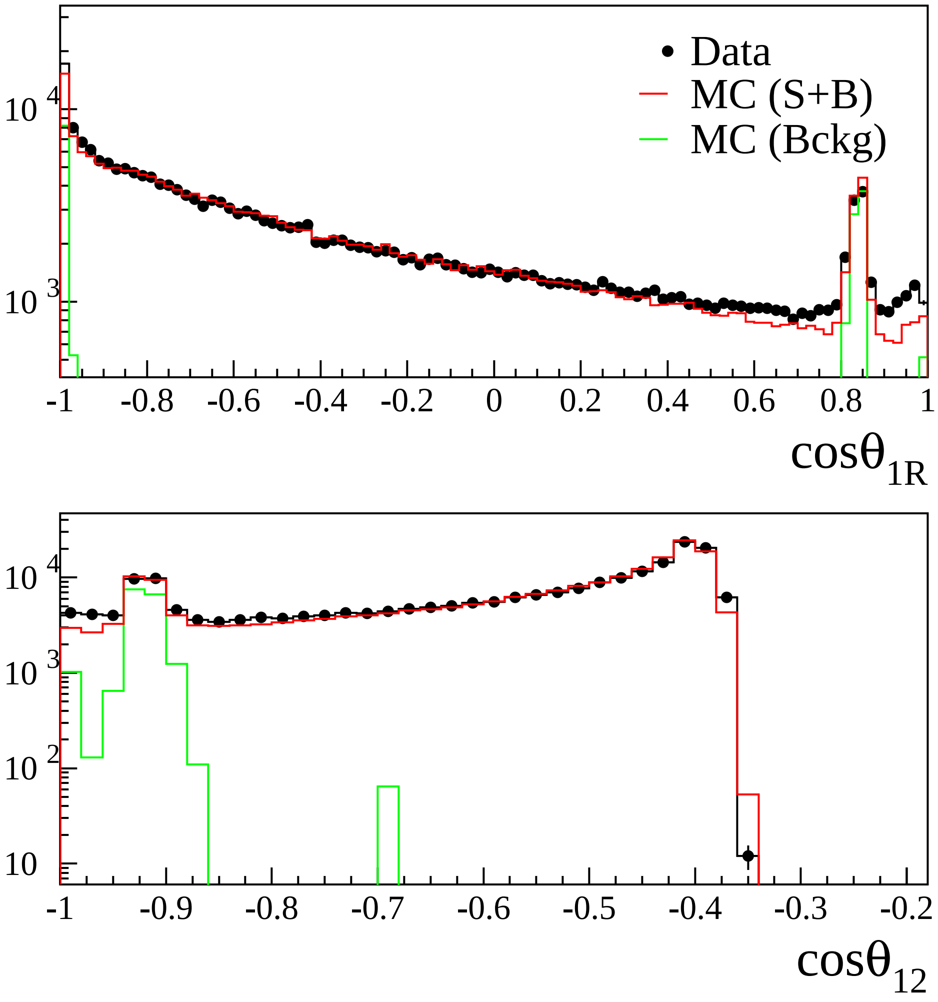

Figure 11: Opening angles for $\phi \to \eta\gamma \to \gamma\gamma\gamma$ events before ΔE cut. 1, 2 are the photons assigned to η while R is the radiative one.

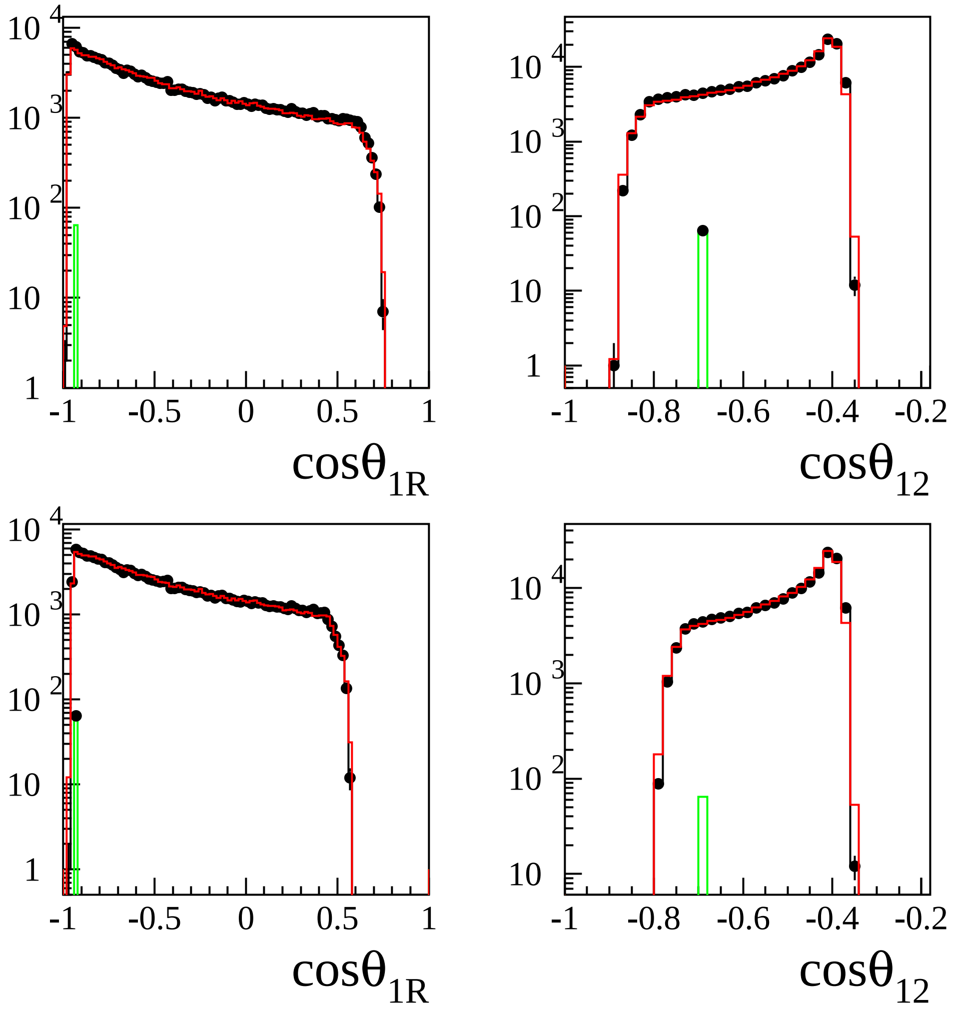

Figure 12: Opening angles for $\phi \to \eta\gamma \to \gamma\gamma\gamma$ events after $|\Delta E| < 330$ MeV (top) and $|\Delta E| < 300$ MeV (bottom) cuts. 1, 2 are the photons assigned to η while R is the radiative one.

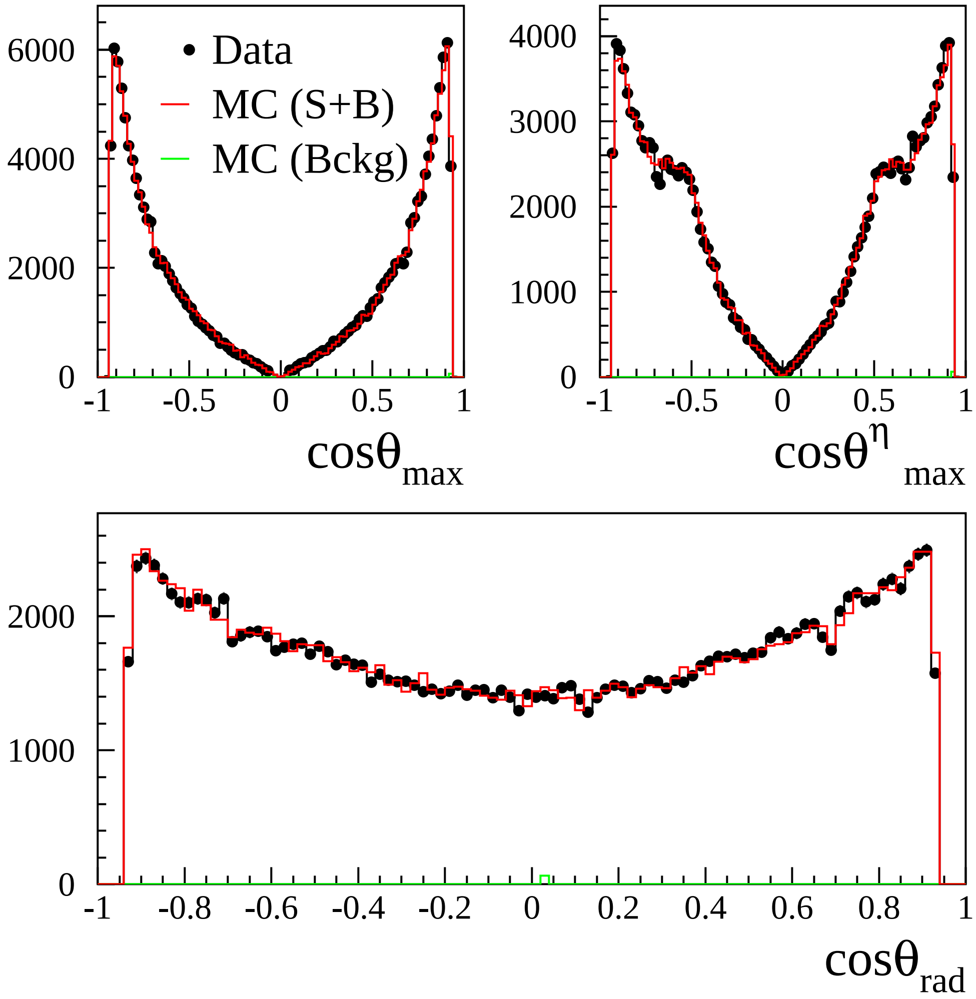

Figure 13: Polar angle distributions for $\phi \to \eta\gamma \to \gamma\gamma\gamma$ events: maximum angle of the event (top-left), maximum angle of the photons assigned to η (top-right) and angle of the radiative photon (bottom).

plateau for energy above 70 MeV and it is stable whenever applying the harder cut-offs (curve (a) of ϵ_{cell}) on the threshold simulation. The effect due to cluster splitting has been reduced to a negligible number using the recover splitting procedure. The merging of close photons is proven by MC not to be an item since the clusters are well separated in space.

- **Angular acceptance**
  Differently from a previous analysis [10], we do not observe any effect due to the angular acceptance. This is shown in Fig. 13 where the distribution of $\theta_{\gamma\,\mathrm{rad}}$ exhibits the expected $(1 + \cos\theta^2)$ dependence.

- **Background contamination**
  A relevant sistematics is given by the evaluation of the residual background since the simulation does not reproduce well the observed rate before applying the ΔE cuts. The background can also be related to accidental overlap of other classes of events with additional machine background clusters; therefore it is important to check the analysis stability whenever changing the angular coverage. In order to do this we evaluated the cross section with $\theta_{\mathrm{cut}} = 21°$, $23°$ on a smaller sample of 1.67 pb^{-1} (samples B, C).

- **Drift chamber related problems**
  To test any eventual effect due to the drift chamber trips we have evaluated the cross-section ignoring all runs whenever even a single trip has been registered by the Slow Control. This restricts sample B to 1.49 pb^{-1} (sample D).

In Tab. 1 we report the number of events counted at the end of the analysis, $N - B$, the selection efficiency and the cross-section for the four samples used. In Tab. 2 the relative systematic errors are summarized.

3.4 Cross section measurement

On sample A, using $\Delta E\mathrm{cut}_2$, we measure:

$$\sigma(\phi \to \eta\gamma \to 3\gamma) = (16.97 \pm 0.05_{\mathrm{stat}} \pm 0.44_{\mathrm{syst}})\ \mathrm{nb} \tag{1}$$

If we consider also the cosmic veto correction of (1.006 ± 0.001) we get:

$$\sigma(\phi \to \eta\gamma \to 3\gamma) = (17.07 \pm 0.05_{\mathrm{stat}} \pm 0.44_{\mathrm{syst}})\ \mathrm{nb} \tag{2}$$

Sample	Variable	No ΔE cut	$\lvert\Delta E\rvert < 330$ MeV	$\lvert\Delta E\rvert < 300$ MeV
A	N-B	206175	179802	163975
	ϵ (%)	73.1 ± 0.1	65.4 ± 0.1	60.3 ± 0.1
	(N-B)/ϵ	281839	274893	271962
	σ (nb)	17.5 ± 0.04	**17.15 ± 0.05**	**16.97 ± 0.05**
B	N-B	21921	19161	17515
	ϵ (%)	73.1 ± 0.1	65.4 ± 0.1	60.3 ± 0.1
	(N-B)/ϵ	29966	29295	29050
	σ (nb)	17.85 ± 0.11	**17.44 ± 0.12**	**17.30 ± 0.13**
C	N-B	20860	17737	16332
	ϵ (%)	69.7 ± 0.1	62.1 ± 0.1	57.2 ± 0.1
	(N-B)/ϵ	29938	29354	29135
	σ (nb)	17.83 ± 0.12	**17.48 ± 0.16**	**17.35 ± 0.14**
D	N-B	19222	16838	15385
	ϵ (%)	73.1 ± 0.1	65.4 ± 0.1	60.3 ± 0.1
	(N-B)/ϵ	26275	25743	25517
	σ (nb)	17.69 ± 0.11	**17.34 ± 0.12**	**17.18 ± 0.13**

Table 1: Analysis output of the four samples with different ΔE cuts: N is the number of events, B the expected background, ϵ the analysis efficiency and σ the $\phi \to \eta\gamma \to \gamma\gamma\gamma$ visible cross section.

Systematic	Relative error (%)
Filfo and NRLOOSE losses	±0.50
ΔE cut (residual background)	±0.58
Acceptance cut (Sample B vs Sample C)	±0.23
DCH trips (Sample B vs Sample D)	−0.69
Stability (Sample A vs Sample B)	±1.22
Luminosity	±2.0
Total	±2.57

Table 2: Systematics for $\sigma(\phi \to \eta\gamma \to \gamma\gamma\gamma)$.

The systematic error is evaluated as the quadrature of all errors listed in Tab. 2.

4 The $\phi \to \eta\gamma \to \pi^0\pi^0\pi^0\gamma$ decay

4.1 Sample selection and background contamination

As a first analysis step, we require the events to have a number of prompt photons, N_γ, in the range $6 \leq N_\gamma \leq 8$. The photon clusters are required to have $E \geq 7$ MeV and to be produced in the angular region $21° \leq \theta \leq 159°$ (ACC cut). Since this is a very clean sample, we do not need to perform any kinematic fit to disentangle data and background. In Fig. 14 the energy distribution of the photons coming from the η and of the radiative photon are shown. A requirement on the photon energy above a high threshold is enough to assign the radiative photon.

For the background we have simulated the two most important contributions:

- **KNEU: $\phi \to K_S K_L \to$ neutrals**
  Events generated by $\phi \to K_S K_L$, with $K_S \to \pi^0\pi^0$ and $K_L \to \pi^0\pi^0\pi^0$, with both kaons decaying at a distance from the origin, R_K, smaller than 10 cm (i.e. inside the beam pipe).
- **KSCH: $\phi \to K_S K_L \to (K_S \to$ charged, $K_L \to$ all)**
  Events generated by $\phi \to K_S K_L$, with $K_S \to \pi^+\pi^-$ and $K_L \to$ everything, with $R_K \leq 10$ cm for both kaons.

The expected background rate/pb^{-1}, N_{bkg}, is estimated as follows:

$$N_{\text{bkg}} = \sigma(\phi) \cdot L_1 \cdot \text{BR}(\phi \to K_S K_L) \cdot \text{BR}_1 \cdot \text{BR}_2 \cdot P_{\text{d}}, \tag{3}$$

where $\sigma(\phi)$ is the visible ϕ production cross section, L_1 is the luminosity of 1 pb^{-1}, $\text{BR}(\phi \to K_S K_L)$ is the BR for the ϕ to decay into $K_S K_L$, BR$_1$, BR$_2$ are the branching ratios for K_S and K_L to the considered final states and, finally, P_{d}, is the probability for the K_L to decay in a sphere of 10 cm radius ($\sim 1 - e^{-R_K/\lambda_{K_L}}$). Using for $\sigma(\phi)$ the value of 3.40 μb, for the branching ratio the values from [11] and for $\lambda_{K_L} = \beta\gamma c\tau = 330$ cm, we get[1] $N_{\text{bkg}} = 2278/\text{pb}^{-1} (23120/\text{pb}^{-1})$ for the two considered backgrounds.

---

[1] For KNEU, $\text{BR}_{\text{tot}} = \text{BR}(\phi \to K_S K_L) \cdot \text{BR}_1 \cdot \text{BR}_2 \cdot P_d$ is equivalent to $\text{BR}_{\text{tot}} = 0.343 \cdot 0.314 \cdot 0.216 \cdot 0.029 = 0.67 \cdot 10^{-3}$; for KSCH $\text{BR}_{\text{tot}} = 0.343 \cdot 0.686 \cdot 0.029 = 6.8 \cdot 10^{-3}$.

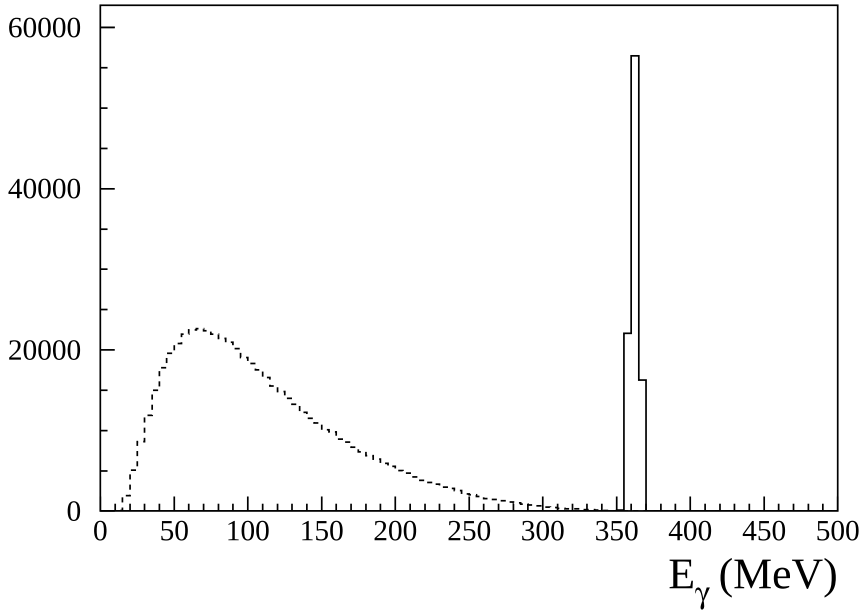

Figure 14: Energy spectra for $\phi \to \eta\gamma \to \pi^0\pi^0\pi^0\gamma$ events: radiative photon (solid) and photons from η (dashed).

We report in Fig. 15 the scatter plots of $E_{\rm tot}$ vs $P_{\rm miss}$ for the events with six or seven prompt photons. On the left side, the scatter plots with black dots represents the data sample while on the right side the distribution for the MC samples is shown. The red-points represent the simulation of the signal while the green (blue) points represent the KNEU (KSCH) background. It is evident that the MC reproduces the main features of the events. In the events with six reconstructed clusters, the elipse of the signal centered at $E_{\rm tot} \sim 650$ MeV and $P_{\rm miss} \sim 350$ MeV corresponds to the cases where the radiative photon is lost since is produced out of angular acceptance. The corresponding plot, in the sample having seven prompt photons, shows this region practically unpopulated since the only events surviving here are due to the coincidence of one cluster splitting and the radiative photon out of acceptance.

To reduce the background contamination we furthermore require the events to satisfy the condition (BOX cut): $E_{\rm tot} \geq 700$ MeV and $P_{\rm miss} \leq 200$ MeV, which corresponds to the box drawn on the scatter plots on the right side of Fig. 15. This last cut has an high efficiency for the signal $\epsilon_{\rm BOX} = 80\%\,(97\%)$ for $N_\gamma = 6\,(7)$ while reduces the KNEU background of a factor 6 (2).

To check if our simulation reproduces the right amount of background, we show in the following few control distributions done before applying the BOX cut. Let us first consider the most difficult case, i.e. the one with 6 prompt photons in acceptance. In Figs. 16.top the distributions of $E_{\rm tot}$ are reported applying $P_{\rm miss} < 200$ MeV (left) or $P_{\rm miss} > 200$ MeV (right). The black line represents the data, the red line the MC expected background + signal contribution. A huge data–MC discrepancy is evident in the region at $E_{\rm tot} < 750$ MeV while the agreement is perfect for $E_{\rm tot} > 800$ MeV; the lower energy region is dominated by KSCH background, but the origin of this discrepancy is not clear. If we arbitrarly scale this background up of a factor 5 we follow satisfactory the peak at 500 MeV and we remain only with a discrepancy in the $600 \div 700$ MeV region. Either we have some reason for a track to cluster efficiency much smaller in the data that in the MC that modifies quickly the photon selection efficiency or we have to consider another background, such as $\phi \to K^+K^-$. For the moment being we consider the background contamination negligible at $E_{\rm tot} > 800$ MeV as shown for the good data–MC agreement in that region. Indeed a similar situation exists if we plot $P_{\rm miss}$ for different values of $E_{\rm tot}$. The distributions in Figs. 16.bottom show indeed a perfect agremeent for a central event while the the same discrepancy of a factor 5 is visible for events with small energy. If we

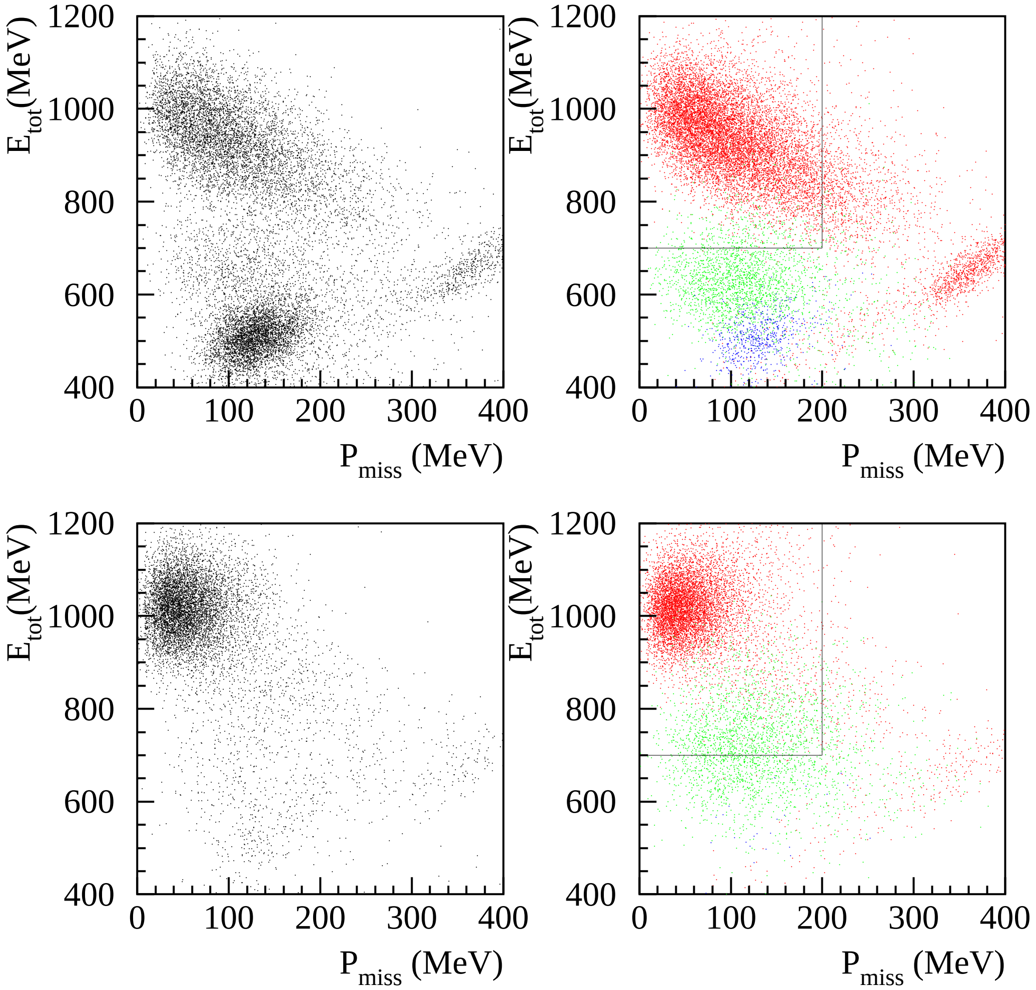

Figure 15: $E_{\rm tot}$ vs $P_{\rm miss}$ distributions for $\phi \to \eta\gamma \to \pi^0\pi^0\pi^0\gamma$ events: data (left) and MC (right) distributions for 6γ's (top) and 7γ's (samples) samples. $\phi \to \eta\gamma \to \pi^0\pi^0\pi^0\gamma$, KNEU and KSCH events are displayed in red, green and blue respectively.

Sample	Cut	6 γ	7 γ	(6+7) γ
ETA7	ACC	$(28.5 \pm 0.2)\%$	$(47.8 \pm 0.2)\%$	$(10.5 \pm 0.3)\%$
ETA7	ACC+EMAX	$(25.5 \pm 0.2)\%$	$(46.5 \pm 0.2)\%$	$(13.4 \pm 0.3)\%$
ETA7	ACC+BOX	$(23.0 \pm 0.2)\%$	$(46.4 \pm 0.2)\%$	$(12.8 \pm 0.3)\%$
ETA7	ACC+BOX+EMAX	$(22.8 \pm 0.2)\%$	$(45.9 \pm 0.2)\%$	$(12.6 \pm 0.3)\%$
KNEU	ACC	$(8.4 \pm 0.1)\%$	$(8.3 \pm 0.1)\%$	$(11.1 \pm 0.1)\%$
KNEU	ACC+EMAX	$(0.6 \pm 0.1)\%$	$(0.5 \pm 0.1)\%$	$(0.9 \pm 0.1)\%$
KNEU	ACC+BOX	$(1.1 \pm 0.1)\%$	$(4.3 \pm 0.1)\%$	$(9.1 \pm 0.1)\%$
KNEU	ACC+BOX+EMAX	$(0.2 \pm 0.1)\%$	$(0.4 \pm 0.1)\%$	$(0.1 \pm 0.1)\%$
KSCH	ACC	$(0.2 \pm 0.1)\%$	$(0.1 \pm 0.1)\%$	0%
KSCH	ACC+EMAX	0%	0%	0%

Table 3: Effect of the analysis cuts on the selection efficiencies for ETA7, KNEU and KSCH samples.

consider instead the sample with 7 prompt photons in acceptance the same plots of $E_{\rm tot}$, $P_{\rm miss}$ are shown in Fig. 17. A good data–MC agreement can be found in this case since the dominating background is due to KNEU and the MC well reproduces the different shapes and rates. As a last check also the sample with 8 prompt photons in acceptance is shown in Fig. 18; the simulation reproduces the event counting also in this case.

As already explained, the selection of the radiative photon is simple for this channel, since it is necessary only to select the photon with higher energy in the event. In Fig. 19 the $E_{\rm max}$ distributions are shown before the BOX cut for the samples with 6, 7 and 8 γ's in acceptance. For the final event counting we require also the condition: $E_{\rm max} > 280$ MeV (EMAX cut). The selection efficiency of finding 6, 7 or 8 prompt photons in the events is reported as a function of different analysis cuts in Tab. 3 for the signal and the two background samples.

In Sample A, we count 51034, 101253 events for 6 and 7 photons in the final state respectively. The control distributions, reported in Figs. 20, 21 and 22 show an excellent data-MC agreement.

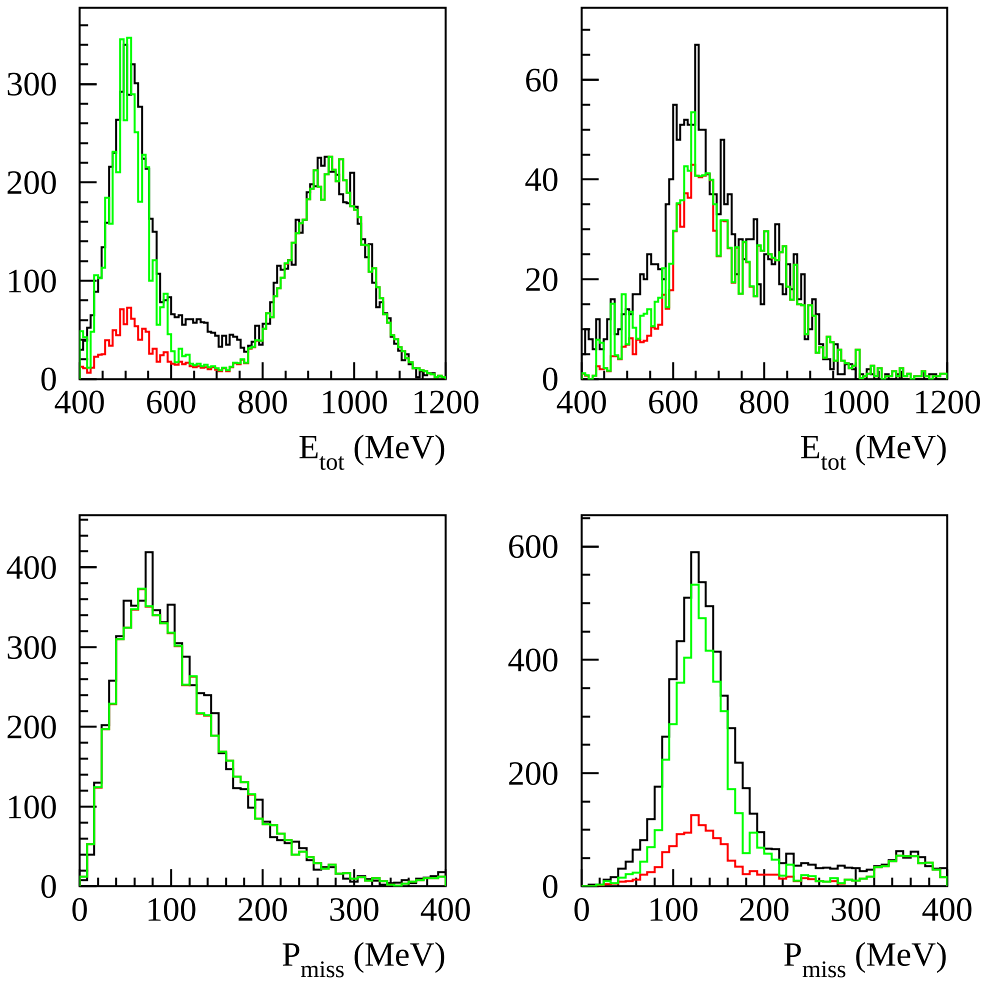

Figure 16: Distributions for the sample with 6 prompt photons: $E_{\rm tot}$ with $P_{\rm miss} \leq 200$ MeV (top-left); $E_{\rm tot}$ with $P_{\rm miss} > 200$ MeV (top-right); $P_{\rm miss}$ with $E_{\rm tot} \geq 700$ MeV (top-left); $P_{\rm miss}$ with $E_{\rm tot} < 700$ MeV (top-right).

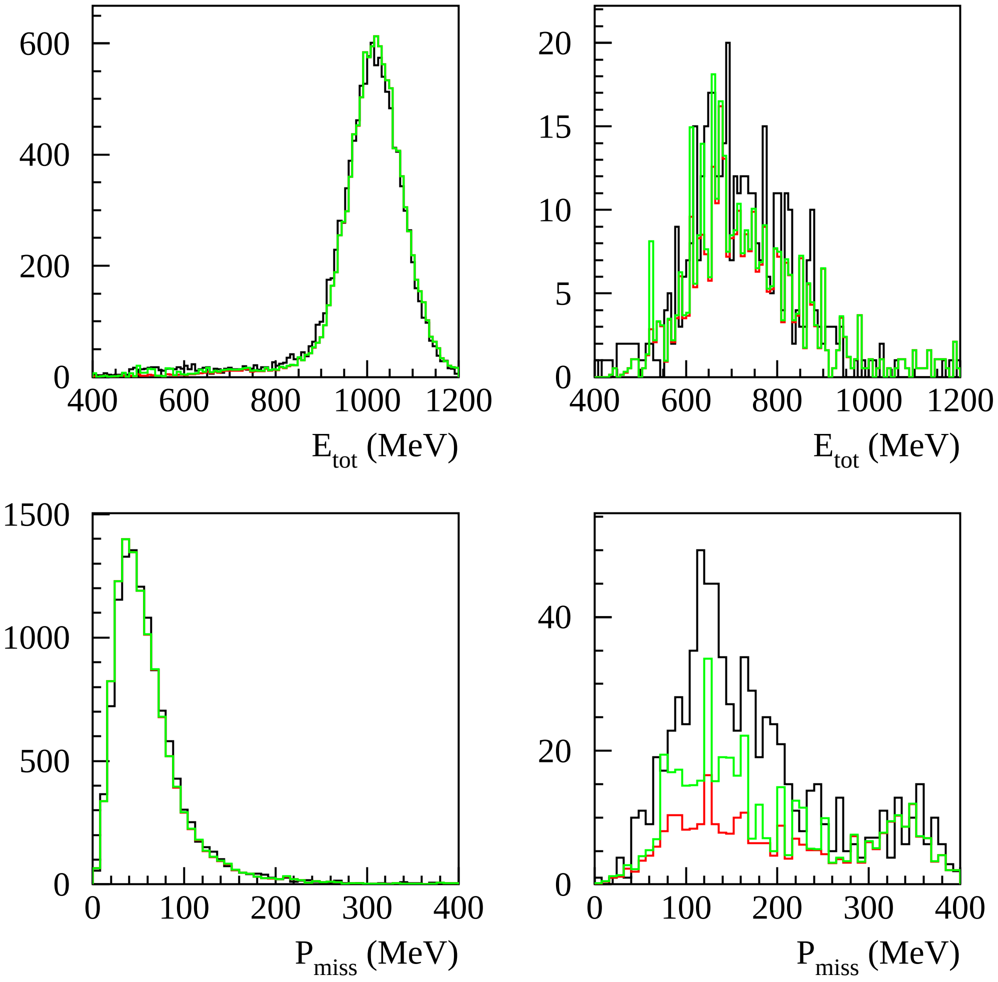

Figure 17: Distributions for the sample with 7 prompt photons: $E_{\rm tot}$ with $P_{\rm miss} \leq 200$ MeV (top-left); $E_{\rm tot}$ with $P_{\rm miss} > 200$ MeV (top-right); $P_{\rm miss}$ with $E_{\rm tot} \geq 700$ MeV (top-left); $P_{\rm miss}$ with $E_{\rm tot} < 700$ MeV (top-right).

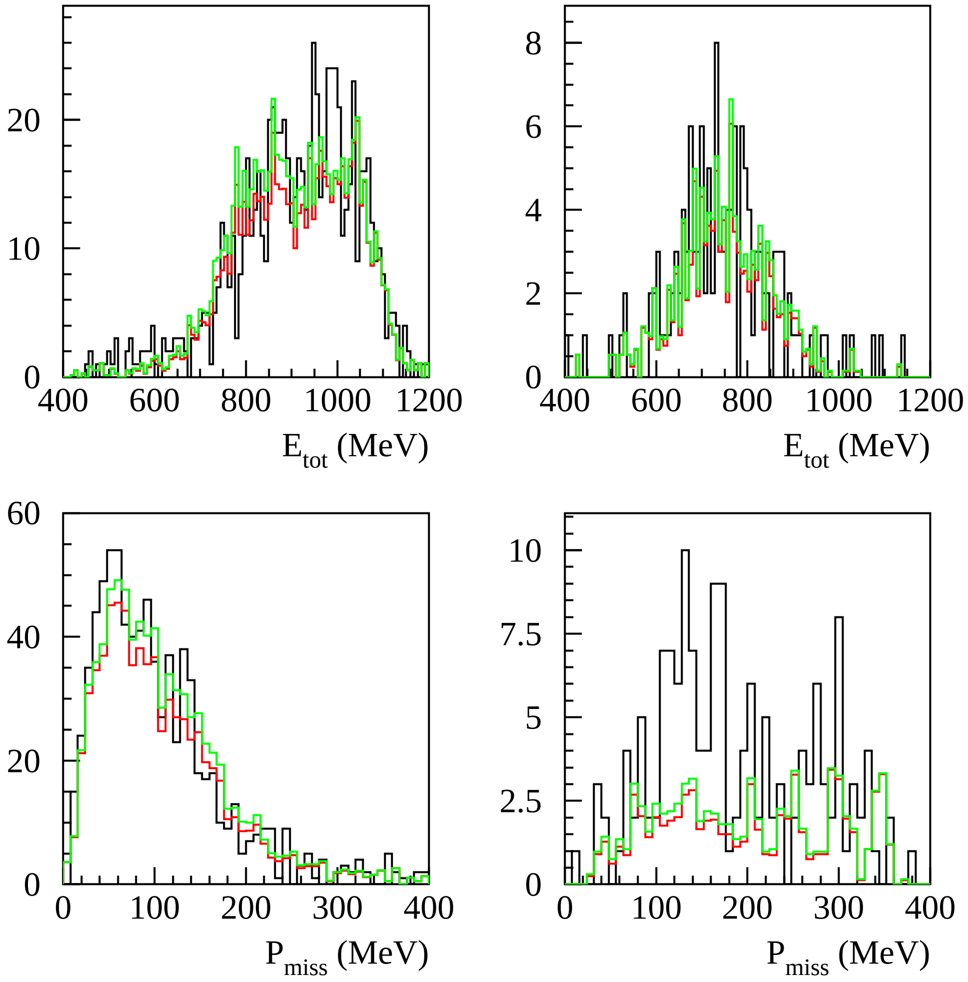

Figure 18: Distributions for the sample with 8 prompt photons: $E_{\rm tot}$ with $P_{\rm miss} \leq 200$ MeV (top-left); $E_{\rm tot}$ with $P_{\rm miss} > 200$ MeV (top-right); $P_{\rm miss}$ with $E_{\rm tot} \geq 700$ MeV (top-left); $P_{\rm miss}$ with $E_{\rm tot} < 700$ MeV (top-right).

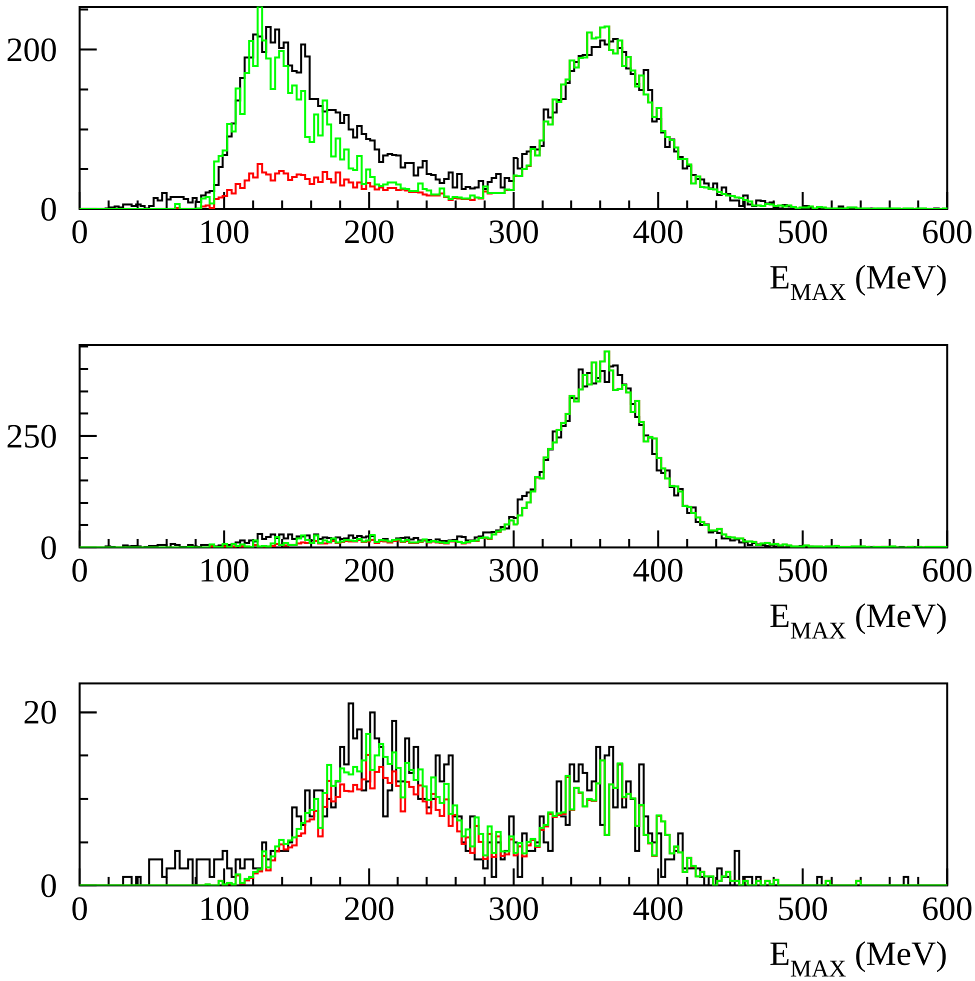

Figure 19: E_{max} before the E_{tot}, P_{miss} cut for events with 6 (top), 7 (middle) and 8 (bottom) prompt photons.

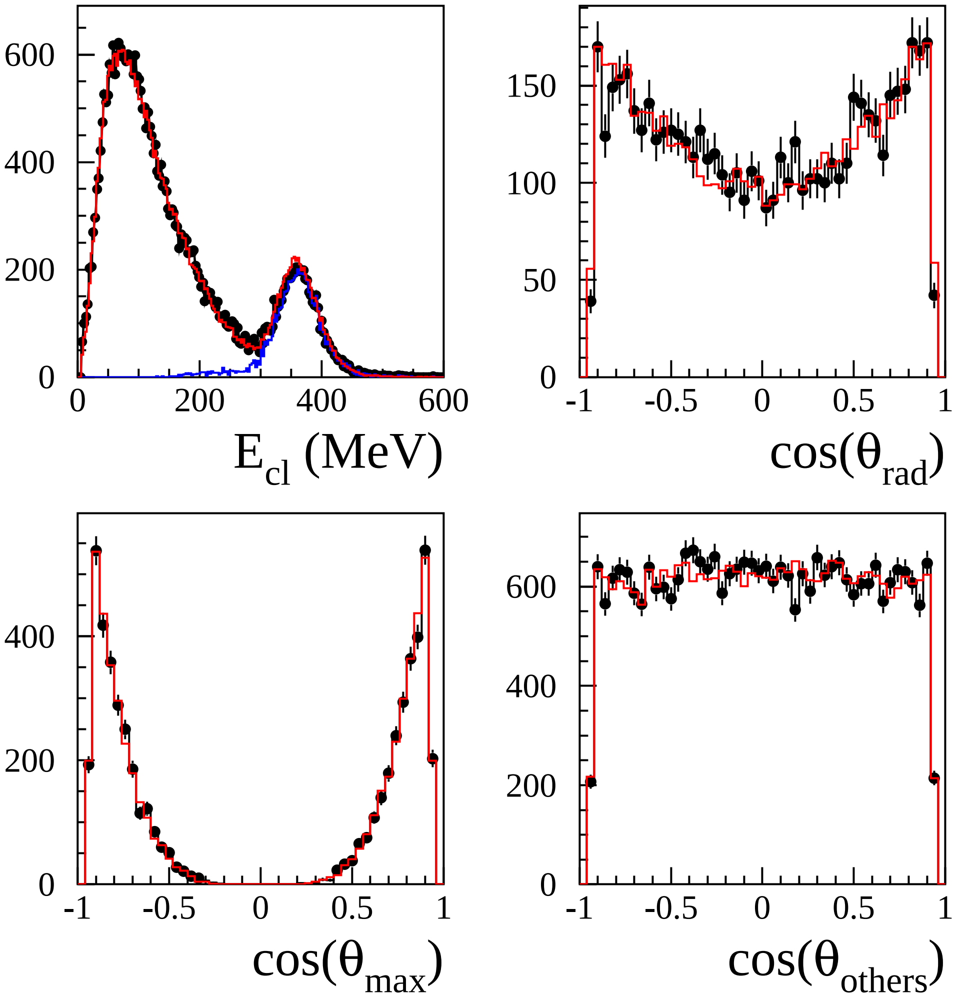

Figure 20: Distributions for the sample with 6 prompt photons: energy of the clusters (top-left), polar angle of the radiative photon (top-right), maximum polar angle of the event (bottom-left) and polar angle of photons from the π^0's decay (bottom-right). Black circles are data, red histograms MC; the blue histogram in (top-left) represents the energy of the radiative photon.

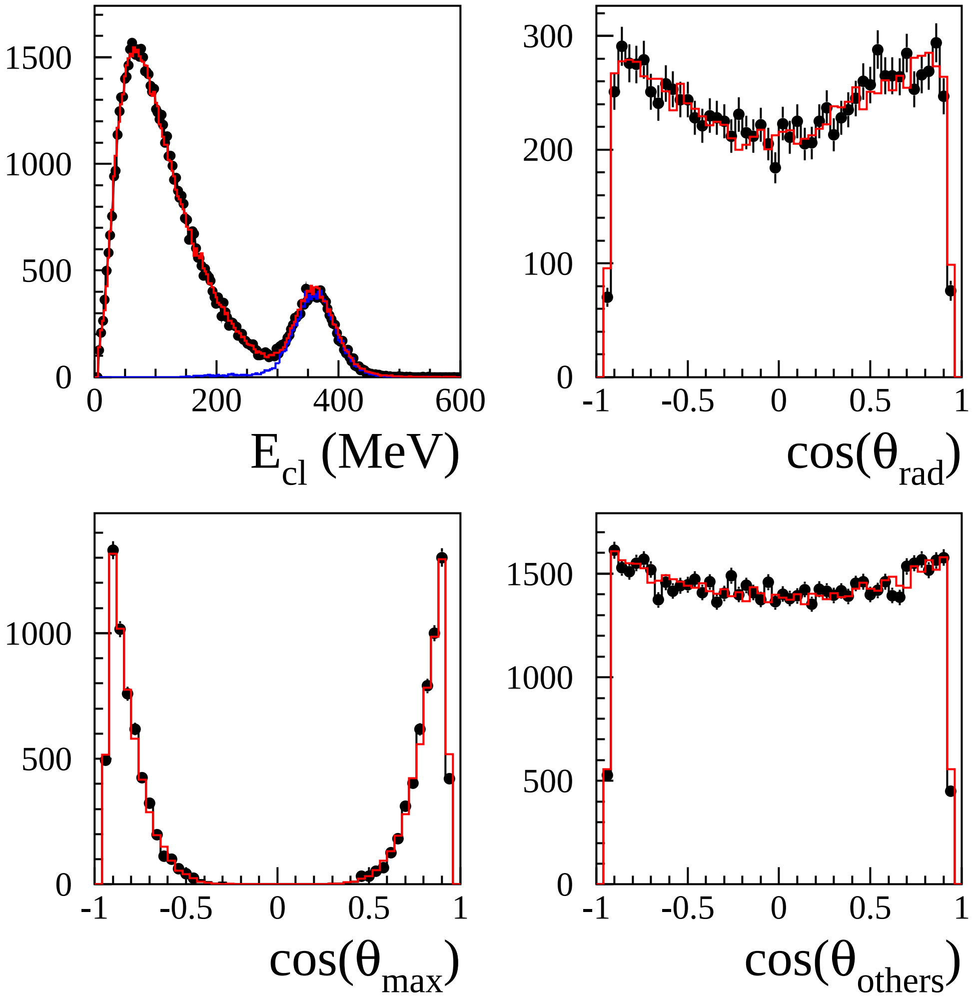

Figure 21: Distributions for the sample with 7 prompt photons: energy of the clusters (top-left), polar angle of the radiative photon (top-right), maximum polar angle of the event (bottom-left) and polar angle of photons from the π^0's decay (bottom-right). Black circles are data, red histograms MC; the blue histogram in (top-left) represents the energy of the radiative photon.

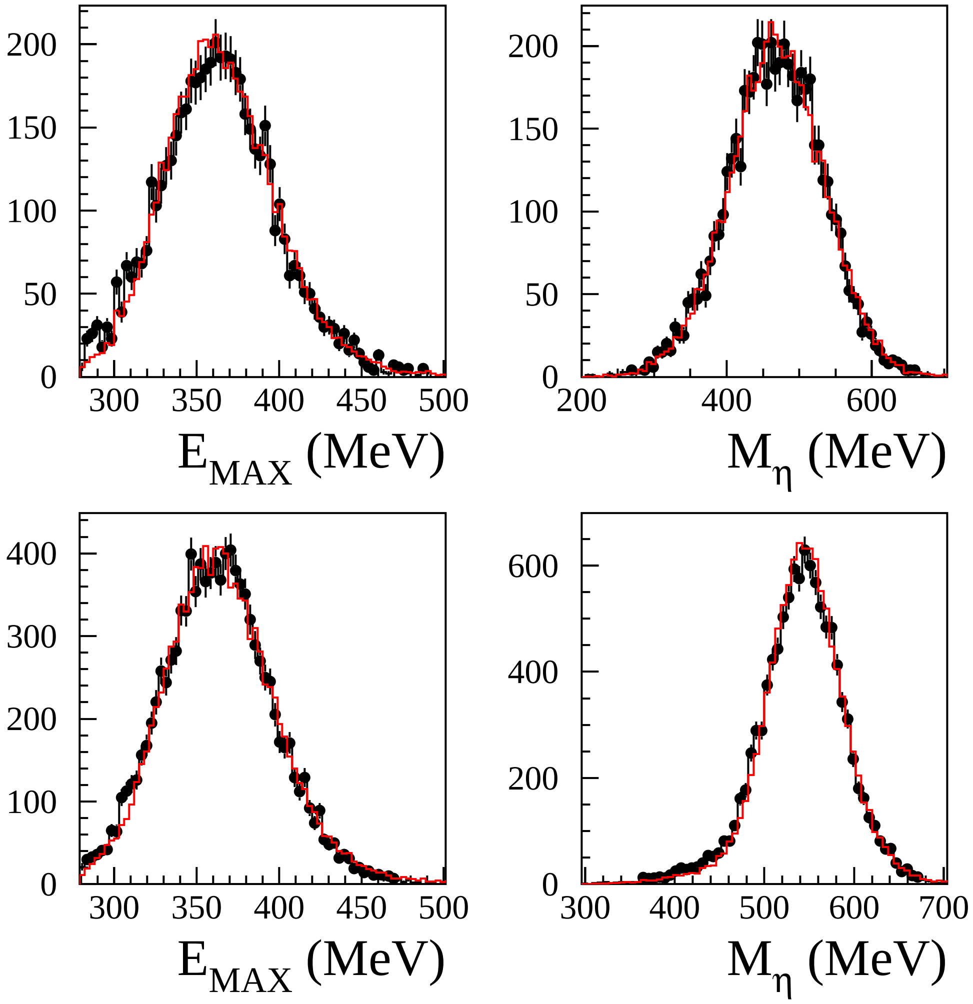

Figure 22: Distributions for the sample with 6 (top) and 7 (bottom) prompt photons: maximum energy of the clusters and η invariant mass.

4.2 Evaluation of the systematic errors

In this paragraph, we discuss the systematics taken into account and we explain the evaluation of the related systematic errors. In order to test the the stability of the analysis varying the analysis cuts or the running conditions we have used the following samples:

- Sample A: whole statistics, standard cuts;
- Sample B: 1.679 pb^{-1} (runs $16103 \div 16292$), standard cuts;
- Sample C: same run range of Sample B, $\theta_{\text{min}} = 23°$;
- Sample D: same run range of Sample B, BOX cut removed;
- Sample E: same run range of Sample B, $\theta_{\text{min}} = 23°$ and BOX cut removed;
- Sample F: same run range of Sample B, runs without trips in the drift chamber.

For each one of these samples, the number of events found, N, the total analysis efficiency, ϵ, and the measured cross section, $\sigma_{\eta 7}$ are reported as a function of N_γ in Tab. 4.

4.2.1 Trigger and event streaming

The efficiency due to the calorimetric ϕ-trigger ($\epsilon_{\phi \text{trg}}$) has been evaluated by MC looking at the events satisfying the whole analysis selection. This efficiency is very high resulting to be: $\epsilon_{\phi \text{trg}} = (99.2 \pm 0.2)\%$. Similarly we expect small losses due to CV since the simulation provides an inefficiency of $\eta_{\text{cv}} = 1 - \epsilon_{\text{cv}} = (0.40 \pm 0.02)\%$.

We have first tested that the simulation reproduces the behaviour of the ϕ-trigger by comparing, between data and MC, the multeplicity-distribution of the fired trigger sectors for the three different calorimeter sub-detectors and the fired trigger-pattern (Figs. 23, 24, 25). The agreement is good and, since the trigger is dominated by triple-coincidence, we consider this error negligible in the following.

The losses due to the cosmic veto can be instead directly measured from the data using the 1/50 vetoed events retained from this purpose in the analysis stream. We observe on Sample A 3/54 159 (3/104 834) events with a cosmic veto flag on the sample with 6 (7) γ's in the final state. This corresponds to an event loss of $(1.9 \pm 0.8) \cdot 10^{-3}$. As in the 3γ's

Sample	Variable	6γ's	7γ's	6γ's+7γ's	8γ's
A	N	51034	101253	152287	3830
	ϵ (%)	22.8 ± 0.1	45.9 ± 0.2	68.7 ± 0.2	1.25 ± 0.04
	(N-B)/ϵ	223181	219920	221000	285840
	$\sigma_{\eta 7}$ (nb)	13.92 ± 0.07	$\mathbf{13.72 \pm 0.06}$	$\mathbf{13.79 \pm 0.05}$	17.83 ± 0.40
B	N	5468	10898	16366	339
	ϵ (%)	22.8 ± 0.1	45.9 ± 0.2	68.7 ± 0.2	1.25 ± 0.04
	(N-B)/ϵ	23915	23672	23752	24990
	$\sigma_{\eta 7}$ (nb)	14.2 ± 0.1	$\mathbf{14.1 \pm 0.1}$	$\mathbf{14.1 \pm 0.1}$	14.9 ± 0.1
C	N	5031	9911	14949	294
	ϵ (%)	20.8 ± 0.1	41.1 ± 0.2	61.9 ± 0.2	1.08 ± 0.03
	(N-B)/ϵ	24083	24074	24077	24866
	$\sigma_{\eta 7}$ (nb)	14.3 ± 0.1	$\mathbf{14.3 \pm 0.1}$	$\mathbf{14.3 \pm 0.1}$	14.8 ± 0.40
D	N	6196	11052	17248	371
	ϵ (%)	25.5 ± 0.1	46.5 ± 0.2	72.0 ± 0.1	1.40 ± 0.04
	(N-B)/ϵ	24206	23714	23888	25807
	$\sigma_{\eta 7}$ (nb)	14.4 ± 0.1	$\mathbf{14.1 \pm 0.1}$	$\mathbf{14.2 \pm 0.1}$	15.4 ± 0.8
E	N	5669	10036	15705	320
	ϵ (%)	23.2 ± 0.1	41.6 ± 0.2	64.8 ± 0.2	1.13 ± 0.03
	(N-B)/ϵ	24329	24088	24174	26126
	$\sigma_{\eta 7}$ (nb)	14.5 ± 0.1	$\mathbf{14.3 \pm 0.1}$	$\mathbf{14.4 \pm 0.1}$	15.6 ± 0.9
F	N	4778	9503	14281	310
	ϵ (%)	22.8 ± 0.1	45.9 ± 68.7	0.1 ± 1.25	0.04
	(N-B)/ϵ	20896	20641	20725	22911
	$\sigma_{\eta 7}$ (nb)	14.1 ± 0.1	$\mathbf{13.9 \pm 0.1}$	$\mathbf{14.0 \pm 0.1}$	15.4 ± 0.9

Table 4: Analysis output of the six samples with a different number of photons in the final state. N is the number of events, B the expected background, ϵ the analysis efficiency and $\sigma_{\eta 7}$ the $\phi \to \eta\gamma \to \pi^0\pi^0\pi^0\gamma$ visible cross section.

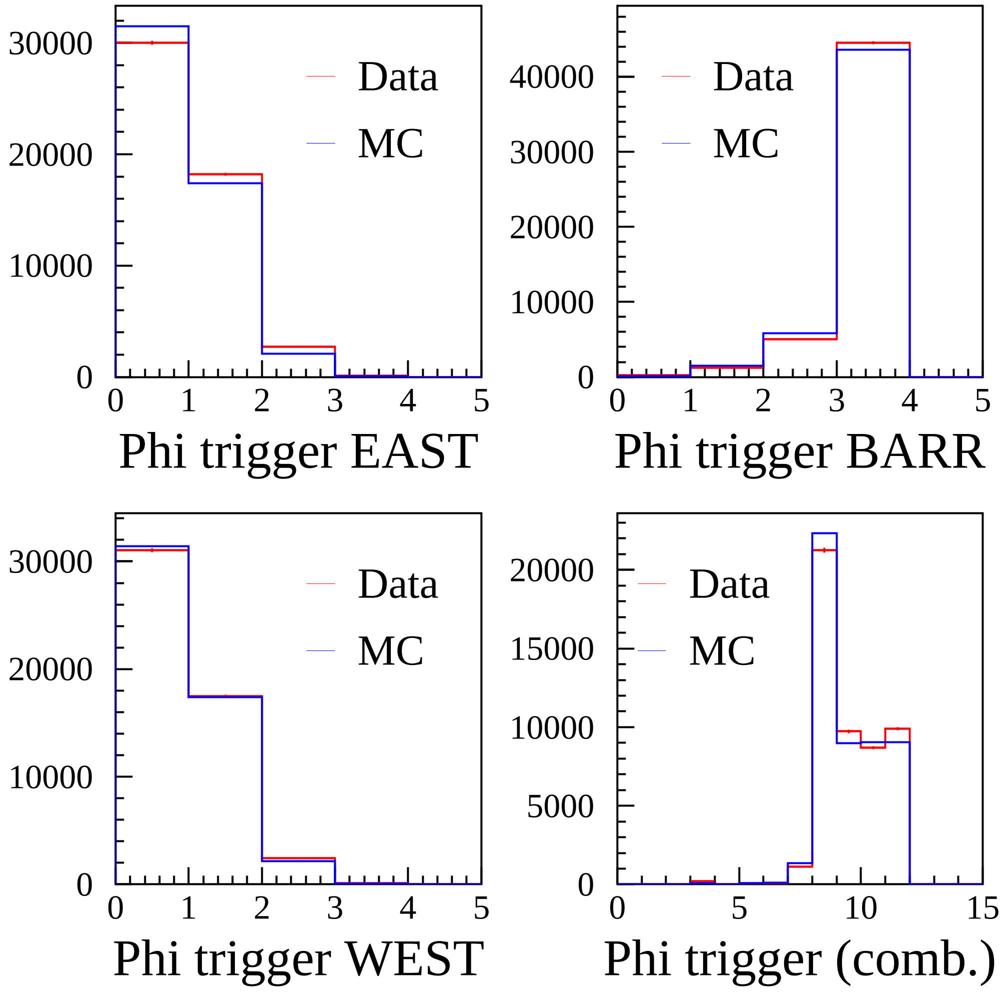

Figure 23: Data and MC trigger distributions for the sample with 6 prompt photons: number of fired LET sectors for Endcap EAST (top-left), Barrel (top-right), Endcap WEST (bottom-left) and LET trigger pattern (bottom-right).

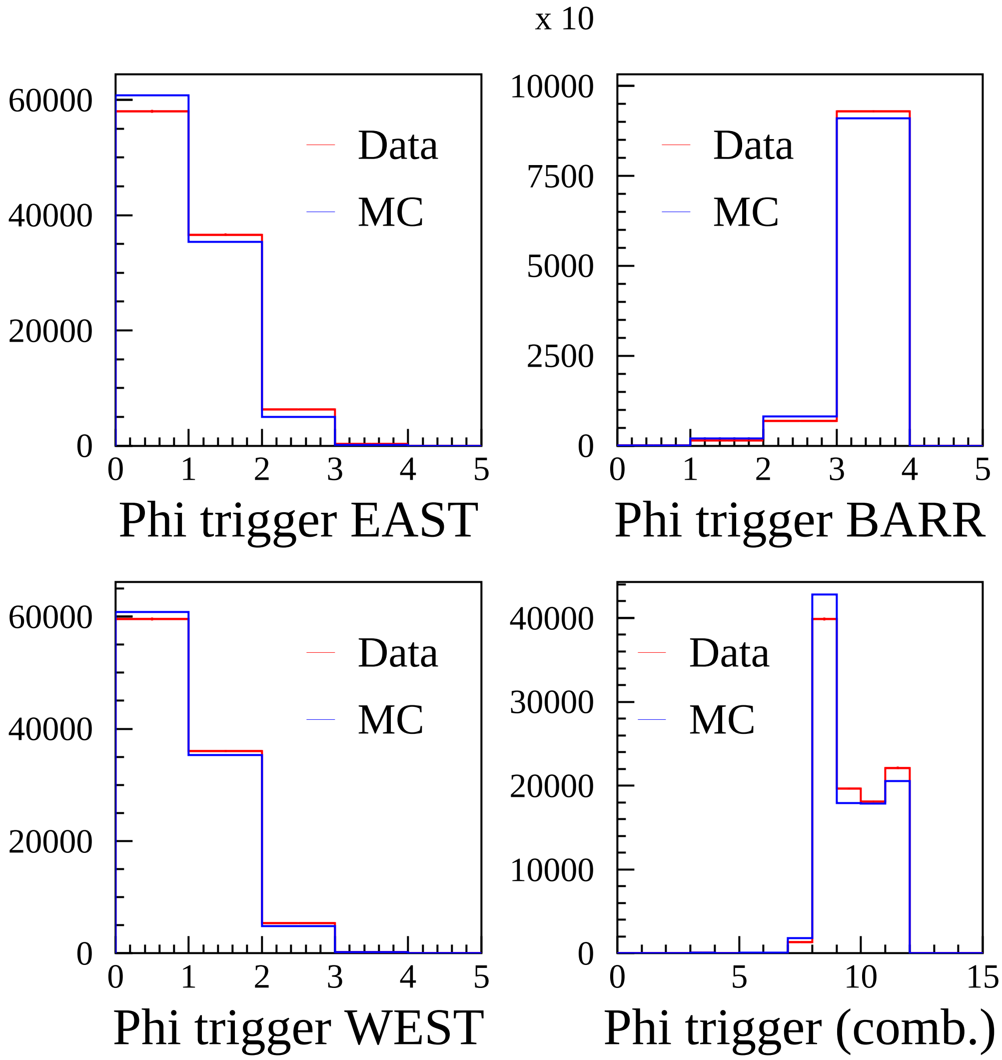

Figure 24: Data and MC trigger distributions for the sample with 7 prompt photons: number of fired LET sectors for Endcap EAST (top-left), Barrel (top-right), Endcap WEST (bottom-left) and LET trigger pattern (bottom-right).

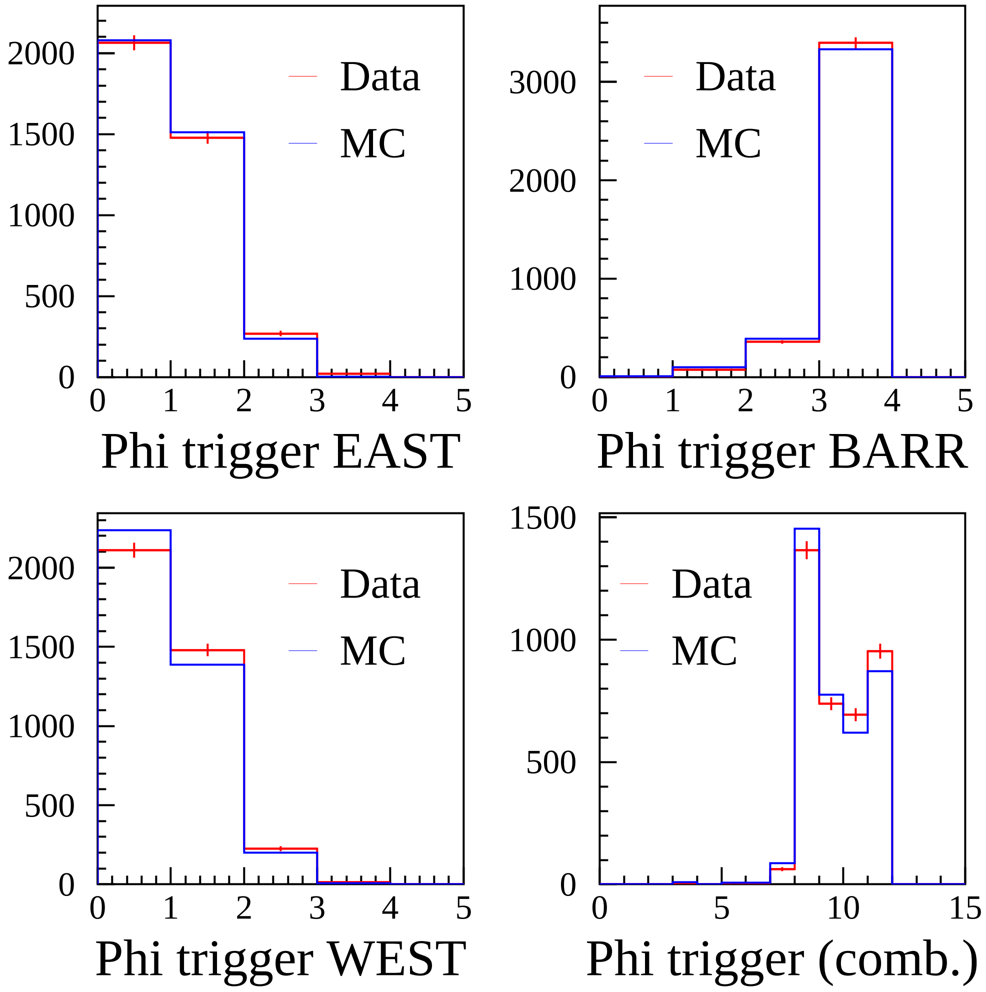

Figure 25: Data and MC trigger distributions for the sample with 8 prompt photons: number of fired LET sectors for Endcap EAST (top-left), Barrel (top-right), Endcap WEST (bottom-left) and LET trigger pattern (bottom-right).

Curve	Threshold	6 γ	7 γ	(6+7) γ
(a)	7 MeV	(23.11 ± 0.14) %	(45.56 ± 0.16) %	(68.68 ± 0.15) %
(b)	7 MeV	(22.76 ± 0.14) %	(45.93 ± 0.16) %	(68.69 ± 0.15) %
(b)	20 MeV	(26.16 ± 0.14) %	(42.25 ± 0.16) %	(68.41 ± 0.15) %

Table 5: MC values of ϵ_{sel} as a function of the N_γ for the two different ϵ_{cell} curves used and increasing the cluster threshold to 20 MeV.

sample, the MC loss is almost twice resulting : $(4.4 \pm 0.3) \cdot 10^{-3}$. This is probably due to a Data-MC difference in the shower profile.

As explained in the introduction, the systematic errors due to the event streaming is related to FILFO and the NRLOOSE selection. After analysis cuts the efficiency of both filters are evaluated by MC to be very high and we have considered these losses negligible.

4.2.2 Cluster counting

The most relevant origin of systematics is related to the cluster counting since the requirement of having 6 or 7 photons in angular acceptance already reduces the selection efficiency to ~ 70 %. Since this is a multiphoton sample with small background contamination, the precision reached on the photon counting translates in showing the stability of the measurement for the visible cross section using an *exclusive photon counting* (i.e. requiring only 6, 7 or 8 photons). The precision of this exclusive measurement is related to the simulation accuracy in describing the clustering details such as: single cluster efficiency, probability of generating a fragment, probability of being merged or having an external accidental contamination. To adapt the reconstruction and the simulation in reproducing the counting in the data we recall the adjustments and the tests done in this analysis:

1. **Accidental simulation**
   The machine background clusters have been simulated inserting the out of time EMC hits in the MC.

2. **Recovery of close shower fragments**
   To count more realistically the fragments produced by the cluster we have used the procedure described in Par. 2.2.

3. **Simulation of the energy threshold**

   A more realistic threshold behaviour at cell level has been introduced in the simulation as described in Par. 2.3. To evaluate the systematic error on the selection efficiency, ϵ_{sel}, we compare, as a function of N_γ, the values found applying in the MC the curves (a) or (b) on ϵ_{cell} (see Tab. 5). The relative error is given as: $\frac{\epsilon_{\mathrm{sel}}(a)-\epsilon_{\mathrm{sel}}(b)}{\epsilon_{\mathrm{sel}}(b)}$ and is of 0.02% in counting 6+7 photons while is at a level of +0.8% for the golden case of 7 photons only.

4. **Effect of the energy scale setting**

   To test the stability of the selection efficiency to the energy dependence of ϵ_{clu}, to any residual effect in the energy scale and to the MC description of accidentals we have determined the cross section, $\sigma_{\eta 7}$, applying a cluster treshold of 20 MeV. A relative systematic error, $\frac{\sigma_{\eta 7}(20)-\sigma_{\eta 7}(7)}{\sigma_{\eta 7}(7)}$, of -0.69%, -0.46%, -0.56% is found when a requirement of 6, 7 and 6+7 photons is used.

5. **T_0 loss due to merging**

   Another effect to be considered is the possibility that the photons impinging on the calorimeter in the same transversal sector, but with different longitudinal positions, merge in a single cluster and alter drastically the timing. We expect such clusters to show a timing faster than the one given by single photons. In this case, these merged clusters can satisfy the condition required by the algorithm providing the T_0 of the event (T_0-finder) and assign a timing earlier than one bunch with the real collision. Whenever this happens, all the other photons (and the event) get lost.

   We have studied such a possibility in the MC looking for clusters composed by at least two primary particles. The distribution of $T-R/c$ for all clusters in acceptance (and without requiring a prompt time window) shows a secondary peak at a multiple of the DAΦNE radiofrequency period ($T_{RF} = +2.715$ ns). To understand the origin of such a bump, we classified the event in 3 categories as a function of N_γ: low ($0 \div 2$), medium ($3 \div 5$), high ($6 \div 8$). For the categories low (high) we plot in Fig. 26.left(right) the $T - R/c$ distribution of all clusters (top), of all clusters with at least one merge candidate (middle) and of all merged clusters (bottom). Indeed, the secondary peak is related to the "early" timing of the merged cluster which satisfies the T_0-finder requirement and is expecially relevant for the low category. The global T_0 loss is estimated by MC counting the class "low" with merged clusters and corresponds to $\sim 1.3\%$ of the generated events.

To control if we have to correct for this effect in the data we compare the distributions of minimum distances for clusters in Barrel and Endcaps in Fig. 27. The data–MC agreement, both in rate and shape, is excellent proving that the simulation reproduce at better than 5% the relative distribution of clusters. Thus the systematic error related to this T_0 loss is completely negligible ($< 0.05 \cdot 0.013 = 0.06\%$).

As a final test we measured $\sigma_{\eta 7}$ using exclusively 6 and 7 or at least 6 reconstructed clusters. The relative error, $\frac{\sigma_{\eta 7}(N_\gamma)-\sigma_{\eta 7}(6+7)}{\sigma_{\eta 7}(6+7)}$, is of $+0.9\%$ (-0.5%) for $N_\gamma = 6(7)$. This is a good result since the exclusive measurement of 7 γ's or the inclusive measurement are consistent at a level of 0.5%.

4.2.3 Angular acceptance

As shown in Fig. 21, the $\theta_{\rm max}$ distribution of the radiative and of the η photons follow closely the MC-shape. The cutoff used in the counting ($\theta_{\rm min} = 21°$) can still suffer of some background contamination at low angles. In order to test the analysis stability as a function of $\theta_{\rm min}$ we have performed the analysis restricting the angular acceptance ($\theta_{\rm min} = 23°$). The stability on $\sigma_{\eta 7}$ is at a level of 0.2 nb/14.1 nb = 1.4%.

4.2.4 Background contamination

To assign an error on the residual background we compare sample B and D where the BOX cut has been removed. The cross-section changes of 0.1 nb/14.1 nb = 0.7%.

4.2.5 DCH trips

To test any eventual effect due to the drift chamber trips we have evaluated the cross-section ignoring all runs whenever even a single trip has been registered by the Slow Control. The cross section changes of: -0.1 nb/14.1 nb = -0.7%.

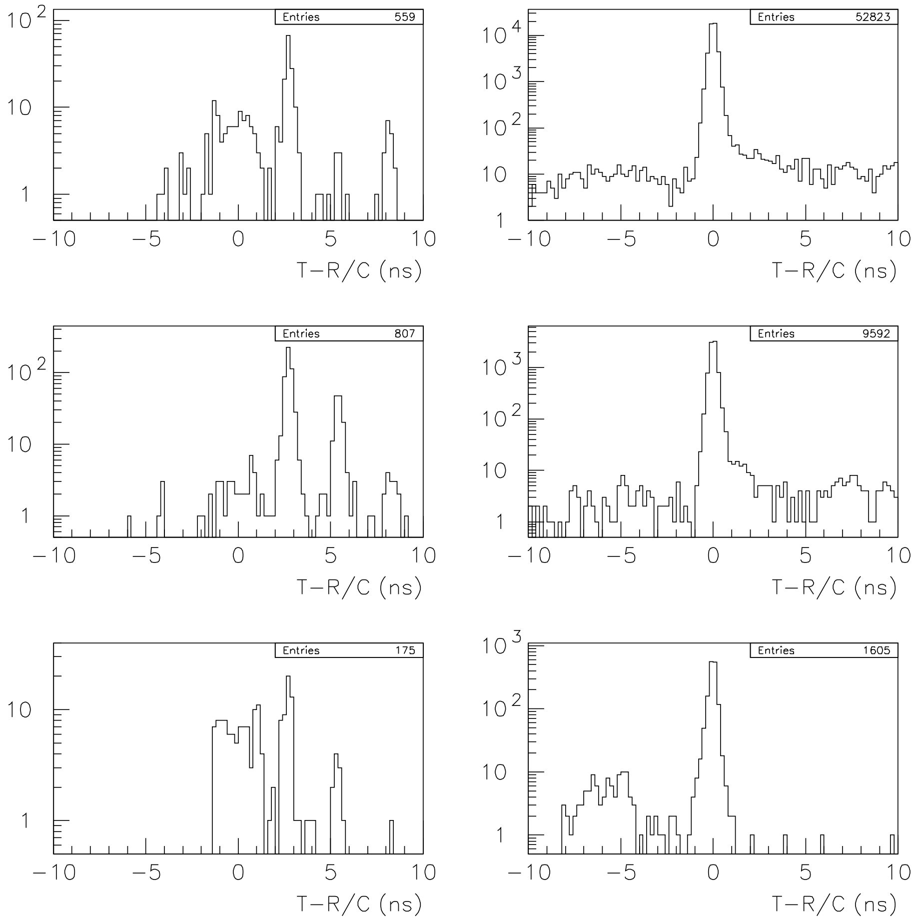

Figure 26: MC distributions of $T - R/c$ for low (left) and high (right) samples: (top) all clusters, (middle) all clusters for events with at least one merged (bottom) all merged clusters.

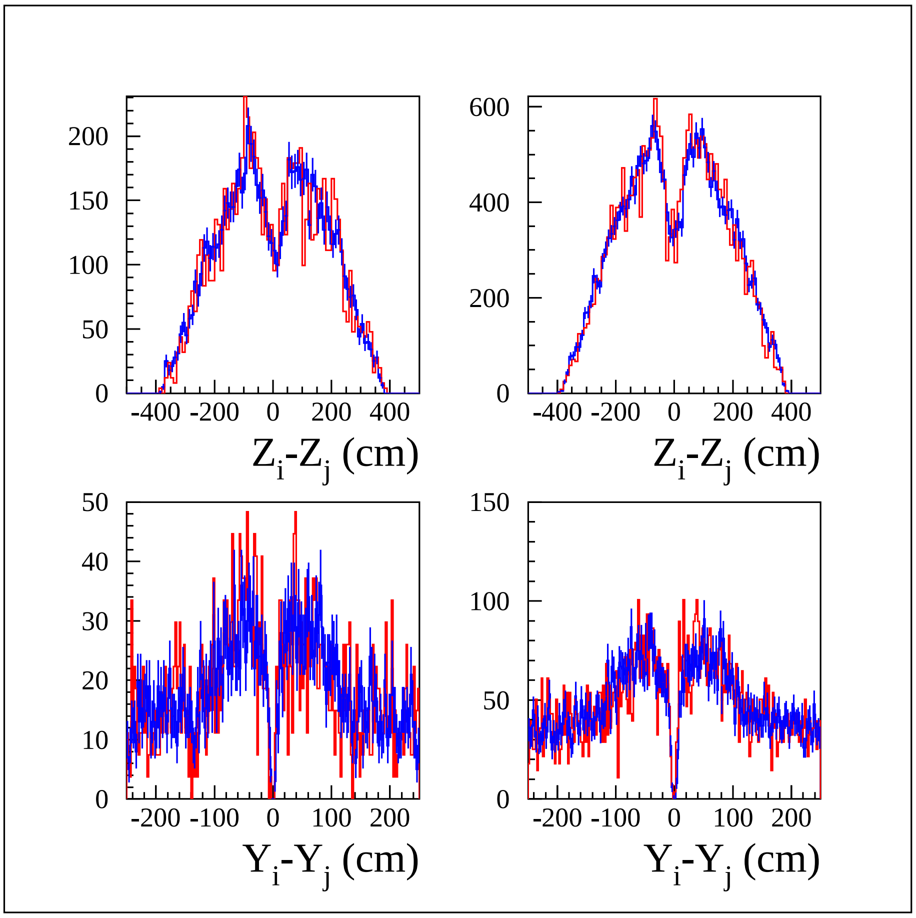

Figure 27: Data–MC comparison of merging for events with N_γ equal to 6 (left) and 7 (right): (top) ΔZ for the closest clusters in the Barrel having $\Delta\phi < 15°$, (bottom) ΔY for the closest clusters in the Endcaps having $\Delta X < 30$ cm.

4.3 Cross section measurement

On the whole sample and without considering the VC correction the cross section is:

$$\sigma(\phi \to \eta\gamma \to 7\gamma) = (13.79 \pm 0.05_{\mathrm{stat}} \pm 0.47_{\mathrm{syst}})\ \mathrm{nb} \tag{4}$$

If we consider also the VC correction of (1.002 ± 0.001) we get:

$$\sigma(\phi \to \eta\gamma \to 3\gamma) = (13.82 \pm 0.05_{\mathrm{stat}} \pm 0.47_{\mathrm{syst}})\ \mathrm{nb} \tag{5}$$

Systematics	Relative error (%)
Clustering	±0.5
Acceptance	±1.4
Background	±0.7
DCH trips	-0.7
Run stability	±2.2
Luminosity	±2.0
Total	±3.4

Table 6: Systematics for $\sigma(\phi \to \eta\gamma \to \pi^0\pi^0\pi^0\gamma)$.

The systematic error is evaluated as the quadrature of the errors explained before and listed in Tab. 6.

5 Ratio of $\mathrm{BR}(\eta \to \gamma\gamma)/\mathrm{BR}(\eta \to \pi^0\pi^0\pi^0)$

The reported measurement of the two cross sections, $\sigma_{\eta 3}$ and $\sigma_{\eta 7}$, can be related to the decay rates of the η into $\gamma\gamma$ and $3\pi^0$. We obtain:

$$R = \frac{\sigma_{\eta 7}}{\sigma_{\eta 3}} = \frac{\mathrm{BR}(\eta \to \pi^0\pi^0\pi^0)}{\mathrm{BR}(\eta \to \gamma\gamma)} = 0.810 \pm 0.026_{\mathrm{stat+syst}} \tag{6}$$

where the luminosity error is not included. This result has to be compared with the PDG value of $R = 0.820 \pm 0.007$ [11] and with the most precise measurement from SND ($R = 0.796 \pm 0.023$) [12].

6 ϕ visible cross section

The measurement of $\sigma_{\eta 3}$ is also used to derive the visible ϕ production cross as follows:

$$\sigma_\phi = \frac{\sigma_{\eta 3}}{\mathrm{BR}(\phi \to \eta\gamma) \cdot \mathrm{BR}(\eta \to \gamma\gamma)} \tag{7}$$

We obtain:

$$\sigma_\phi = (3.34 \pm 0.01_{\mathrm{stat}} \pm 0.12_{\mathrm{syst}})\ \mu\mathrm{b} \tag{8}$$

where the systematic error takes into account the relative errors of: 2.57% on $\sigma_{\eta 3}$, 2.32% from PDG and 1.2% error from the discrepancy between $\sigma_{\eta 3}$ and $\sigma_{\eta 7}$.

7 Conclusions

A precise measurement of the visible cross section for the relative abundant decay $\phi \to \eta\gamma$ has been carried out in two different channels ($\eta \to \gamma\gamma$, $\eta \to \pi^0\pi^0\pi^0$). The ratio of the BR between these two decay channels shows a nice agreement with previous measurements. The ϕ visible cross-section at the ϕ-peak is determined to be:

$$\sigma_\phi = (3.34 \pm 0.01_{\text{stat}} \pm 0.12_{\text{syst}})\ \mu\text{b} \tag{9}$$

References

[1] A. Denig, KLOE Physics Workshop at la Biodola, 23th-25th May 2001 (*http://www.lnf.infn.it/kloe/private/biodola/denig.pdf*) and private communication.

[2] S. Giovannella and S. Miscetti, KLOE Note 178 (2002).

[3] C. M. C. Calarne *et al.*, Nucl. Phys. B 584 (2000) 459.

[4] G. Cabibbo, “Misura di $\Gamma(K_S \to \pi^+\pi^-)/\Gamma(K_S \to \pi^0\pi^0)$ con il rivelatore KLOE”, PhD thesis, Università degli Studi di Roma “La Sapienza” (2000), unpublished.

[5] S. Miscetti and T. Spadaro, KLOE Memo 251 (2001).

[6] S. Miscetti, KLOE Memo in writing.

[7] M. Adinolfi *et al.*, Nucl. Instr. Meth. A 482 (2002) 363-385.

[8] A. Aloisio *et al.*, “Calibration of the KLOE Electromagnetic Calorimeter”, Proc. of the 10th International Conference on Calorimetry in High Energy Physics, Pasadena, CA, USA, 25–30 March 2002.

[9] S. Dell’Agnello and M. Primavera, KLOE Memo 221 (2000).

[10] F. Scuri, KLOE Memo 217 (2000).

[11] D. E. Groom *et al.*, The European Physical Journal C15 (2000).

[12] M. N. Achasov *et al.*, The European Physical Journal C12 (2000) 25.